CDF/ANAL/JET/CDFR/**6854**
Version 1.0
February 17, 2004

Relative jet energy corrections using missing E_T projection fraction and dijet balancing

A. A. Bhatti[1], K. Hatakeyama[2]

The Rockefeller University, New York, NY 10021

Abstract

The relative jet energy corrections are applied to raw jet energies measured in the calorimeter to make the calorimeter response to jet energies uniform in η. In Run 1, the missing E_T projection fraction (MPF) was used to obtain the corrections; however, in Run 2 the p_T balancing of the leading two jets (Δp_T) in dijet events has been used. In this note, the corrections obtained from the two methods are compared. The corrections obtained from the two methods are found to be different by ~ 2 % in the region of $1 \lesssim \eta \lesssim 2$, which can be explained by the difference between central and plug jets in the energy leakage outside the jet cone due to cascade showers in the calorimeter. The leakage effect is taken into account by the Δp_T method, but not by the MPF method; therefore, the Δp_T method is the more appropriate method to use to obtain the relative jet energy corrections.

[1]bhatti@fnal.gov
[2]hatake@fnal.gov

Contents

1 Introduction

The raw jet energies measured in the calorimeters have to be corrected for detector effects before they are compared to predictions from the theoretical models. The *generic jet energy corrections* to be applied to jets in the CDF Run 2 data were obtained and described in detail elsewhere [1, 2]. Briefly, the generic jet energy corrections include:

- Relative energy corrections which correct jets back to an equivalent jet in the η range of $0.2 < |\eta| < 0.6$ to make the calorimeter response uniform in η,

- Multiple $p\bar{p}$ interaction corrections which subtract the energy due to additional $p\bar{p}$ interactions from the jet energy,

- Absolute jet energy corrections which convert the calorimeter cluster p_T to the $\sum p_T$ of particles in the cone (calorimeter energy to particle energy),

- Underlying event corrections which subtract the energy due to underlying event (fragmentation of partons which are not associated with the hard scattering) from the jet energy,

- Out-of-cone corrections which accounts for the energy that leaks outside the jet cone due to fragmentation effects and soft gluon radiation.

The generic jet energy corrections are comprised of several steps in order to allow people to use a subset of them depending on their physics analyses.

This note presents a study of the relative jet energy corrections which correct jets for any variation with detector-η. The corrections are obtained using the property that two jets should be balanced in p_T apart from the effects of a soft third jet. In order to obtain the corrections, we define a jet with $0.2 < |\eta| < 0.6$ as a **trigger jet** and define the other jet as a **probe jet**. When both jets are in the region of $0.2 < |\eta| < 0.6$, the trigger and probe jets are assigned randomly. The p_T balancing fraction $\Delta p_T f$ is then formed:

$$\Delta p_T f \equiv \frac{\Delta p_T}{p_T^{ave}} = \frac{p_T^{probe} - p_T^{trigger}}{(p_T^{probe} + p_T^{trigger})/2}. \tag{1}$$

The correction factor to make, *on average*, the p_T^{probe} scale equal to $p_T^{trigger}$ is given by:

$$\beta(\Delta p_T) \equiv \frac{p_T^{probe}}{p_T^{trigger}} = \frac{2+ < \Delta p_T f >}{2- < \Delta p_T f >} \tag{2}$$

This method is referred to as the $\boldsymbol{\Delta p_T}$ **method** throughout this note. Please note that, for convenience, the definition of β is inversed with respect to the one in Ref. [3].

In Run 1, the missing E_T projection fraction (MPF) along the probe jet defined as

$$MPF = \frac{\overrightarrow{\not{E}_T} \cdot \overrightarrow{p_T^{probe}}}{(p_T^{probe} + p_T^{trigger})/2} \tag{3}$$

was used to obtained to the relative jet energy corrections [3, 4]. If there is no soft gluon radiation and the underlying event is perfectly balanced in the transverse plane,

$$\overrightarrow{\not{E}_T} \cdot \overrightarrow{p_T^{probe}} = p_T^{trigger} - p_T^{probe}, \tag{4}$$

so that the the correction factor is

$$\beta(MPF) \equiv \frac{p_T^{probe}}{p_T^{trigger}} = \frac{2- < MPF >}{2+ < MPF >}. \tag{5}$$

This **MPF method** has been claimed to be “less dependent on how well the third jet is clustered and results in a better dijet balancing resolution” (see CDFnote-835 [5]). This can be easily understood by considering a situation such as the one shown in figure 1. When there is a third jet as shown in figure 1, obviously the leading two jets do not balance; however, the missing E_T should be still zero. Therefore, the MPF method is expected to have a better balancing resolution and be less sensitive to third jet effects.

Nevertheless, the MPF method has not been used in Run 2 because the missing E_T in the CDF Run 2 data was not well understood when the Run 2 jet correction studies were started. Now, the missing E_T in the CDF Run 2 data is much better understood (see e.g. CDFnote-6112); therefore, it would be nice to compare the corrections from the Δp_T and MPF methods and see which method yields the better and more appropriate corrections.

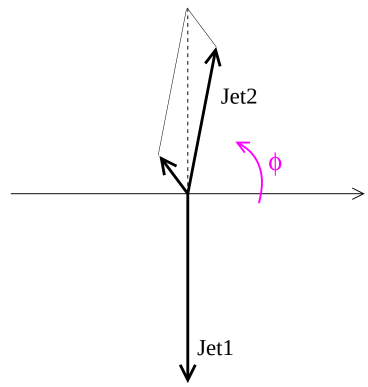

Figure 1: Schematic drawing of two high p_T jets associated with a soft gluon radiation in the transverse plane.

2 Data sets and event selections

In this study, the stntuples for the four data sets, Jet_20, Jet_50, Jet_70 and Jet_100 processed with the offline version 4.10.4 are used. The run interval used is 138819-165439 which corresponds to the period of February 9, 2002 to June 30, 2003. The following event selections, which are basically the same as those used to obtain the generic jet energy corrections [1, 2], were applied to the data samples in this study unless otherwise noted. In order to study the dependence of the jet corrections on the event selections, the cut thresholds are changed in some cases. In those cases, the applied cuts are explicitly mentioned.

1. Good runs (using the good run list for "QCD no silicon" version 4.0 from the DQM group [6]),
2. Number of jets, $N_{jets} \geq 2$,
3. Missing E_T significant, $\not{E}_T/\sqrt{\sum E_T} < 3$,
4. At least one jet with $0.2 < |\text{detector-}\eta| < 0.6$,
5. $|z_{vertex}| < 60$ cm,
6. The azimuthal angle between the leading two jets, $\Delta\phi(jet1, 2) > 2.5$ radians,
7. Average p_T of the leading two jets, $p_T^{ave,min} < p_T^{ave}(jet1, 2) \equiv (p_T^{jet1} + p_T^{jet2})/2 < p_T^{ave,max}$ GeV/c,
8. p_T of the third jet, $p_T(jet3) < p_T^{jet3,max}$ GeV/c.

Distributions of number of jets, missing E_T significance, z_{vertex} and $\Delta\phi(jet1, 2)$ before and after the selection cuts are shown in figures 2, 3, 4 and 5 for the Jet_20, 50, 70 and

Table 1: Selection cuts used for the four different data sets.

Data Set	$p_T^{ave,min}$ (GeV/c)	$p_T^{ave,max}$ (GeV/c)	$p_T^{jet3,max}$ (GeV/c)
Jet_20	25	55	8
Jet_50	55	75	8
Jet_70	75	105	10
Jet_100	105	200	10

100 data samples (cone size $R = 0.7$), respectively. Distributions of $p_T^{ave}(jet1, 2)$ and p_T of the leading three jets are also shown in figures 2, 3, 4 and 5. The cut thresholds on $p_T^{ave}(jet1, 2)$ and $p_T(jet3)$, i.e. $p_T^{ave,min}$, $p_T^{ave,max}$ and $p_T^{jet3,max}$ depend on the data set and are given in table 1.

The $\Delta\phi$ and $p_T(jet3)$ cuts are applied to select events with smaller third jet activities which will spoil the p_T balancing between the leading two jets. The effect of the $p_T(jet3)$ cut can be seen in figures 6, 7, 8 and 9. In these figures, it is seen that the missing E_T vector is running in the direction of the next-to-leading jet more frequently than in the leading jet direction as naively expected. The tendency becomes more prominent as the cut on $p_T(jet3)$ becomes tighter. The number of events which pass each selection cut are summarized in table 2.

Table 2: Number of events after each event selection cut for the four different data sets and three different jet cone sizes.

	Jet_20			Jet_50		
	$R = 0.7$	$R = 0.4$	$R = 1.0$	$R = 0.7$	$R = 0.4$	$R = 1.0$
Good runs	7,181,798			3,139,922		
$N_{jets} \geq 2$	7,154,050	7,140,464	7,155,421	3,108,559	3,108,894	3,106,798
$\not{E}_T/\sqrt{\sum E_T} < 3$	7,144,660	7,126,839	7,146,560	3,079,539	3,079,538	3,079,539
1 jet, $0.2 < \lvert\eta\rvert < 0.6$	2,518,017	2,499,902	2,497,898	1,340,425	1,331,713	1,338,635
$\lvert z_{vertex}\rvert < 60$ (cm)	2,371,696	2,355,283	2,353,451	1,264,751	1,256,347	1,263,190
$\Delta\phi(jet1, 2) > 2.5$	1,969,357	1,869,984	1,974,886	1,187,996	1,159,730	1,194,700
$p_T^{ave}(jet1, 2)$ cut	509,068	244,886	852,659	321,152	196,764	442,657
$p_T(jet3) < p_T^{jet3,max}$	222,788	147,095	268,055	113,369	88,289	129,140
$p_T(jet3) < 5$ GeV/c*	100,297	81,137	129,221	54,556	49,058	68,360
	Jet_70			**Jet_100**		
	$R = 0.7$	$R = 0.4$	$R = 1.0$	$R = 0.7$	$R = 0.4$	$R = 1.0$
Good runs	1,424,112			1,720,717		
$N_{jets} \geq 2$	1,386,223	1,386,932	1,383,850	1,578,861	1,582,805	1,569,491
$\not{E}_T/\sqrt{\sum E_T} < 3$	1,353,443	1,353,443	1,353,443	1,467,882	1,467,882	1,467,882
1 jet, $0.2 < \lvert\eta\rvert < 0.6$	648,676	645,036	648,742	786,945	782,861	787,768
$\lvert z_{vertex}\rvert < 60$ (cm)	612,011	608,647	612,269	742,360	738,607	743,158
$\Delta\phi(jet1, 2) > 2.5$	586,184	575,587	589,420	720,476	710,620	724,454
$p_T^{ave}(jet1, 2)$ cut	187,990	122,980	245,218	294,804	205,009	369,177
$p_T(jet3) < p_T^{jet3,max}$	62,923	50,467	71,939	96,308	77,689	112,728
$p_T(jet3) < 5$ GeV/c*	31,235	28,501	39,742	49,645	44,720	64,489

* This cut is applied only when the dependence on the p_T^{jet3} cut is studied.

3 Comparisons between the Δp_T and MPF methods

In this section, comparisons between the relative jet energy corrections from the Δp_T and MPF methods are presented. Details of the two methods are described in Section 1. The $\Delta p_T f$ and MPF are defined in Eqs. (1) and (3), respectively.

3.1 Shape of the $\Delta p_T f$ and MPF distributions

Figures 10 and 11 show $-$MPF and $\Delta p_T f$ distributions[3] for all the detector-η bins in the Jet_20 data (cone size $R = 0.7$). In all the detector-η bins, MPF distributions are narrower than $\Delta p_T f$ distributions, which is consistent with results from the study in Run 0 [5]. Figure 12 shows the enlarged version of one of the plots in figure 10 and the RMS of the MPF and $\Delta p_T f$ distributions as a function of detector-η. The RMS of the MPF distributions is smaller than that of the $\Delta p_T f$ distributions by roughly 20% for the cone size of $R = 0.7$ in the Jet_20 data.

3.1.1 For different cone sizes

Figures 13 and 14 are the same as figures 12 but for the cone sizes of $R = 0.4$ and 1.0, respectively. In both cases, the RMS of the MPF distributions is again smaller than that of the $\Delta p_T f$ distributions. The difference in the RMS is about 30 % for the cone size of $R = 0.4$ and about 15 % for $R = 1.0$. This can be explained by the fact that the smaller cone size is more sensitive to the soft gluon radiation.

3.1.2 Dependence on the $\Delta\phi(jet1, 2)$ and $p_T(jet3)$ cuts

Please note that the selection cuts $\Delta\phi(jet1, 2) > 2.5$ and $p_T(jet3) < 8$ GeV/c are applied to event used in figures 10-14 to reduce the effect of the gluon radiation. Figure 15 is the same as figure 12 but the $\Delta\phi(jet1, 2) > 2.5$ and $p_T(jet3) < 8$ GeV/c cuts are not applied. When these two selection cuts are not applied, $\Delta p_T f$ distributions become wider; on the other hand, MPF distributions do not change significantly.

3.1.3 For different jet p_T's

Comparisons between the MPF and $\Delta p_T f$ distributions and the RMS of them as a function of detector-η for the Jet_50, 70 and 100 data are shown in figures 16, 17 and 18, respectively. The difference between the MPF and $\Delta p_T f$ distributions is smaller at higher jet p_T's; however, the RMS of the MPF distributions is always systematically smaller than that of the Δp_T distributions, and the difference is larger for smaller cone sizes.

[3] When there is no soft gluon radiation etc, $\Delta p_T f = -MPF$; therefore, $-$MPF distributions are compared with $\Delta p_T f$ distributions. However, $-$MPF distributions are sometimes referred to as MPF distributions for simplicity.

3.2 Relative jet energy corrections from the Δp_T and MPF methods

Figure 19 shows the correction factors $\beta(MPF)$ and $\beta(\Delta p_T)$, which are obtained from the MPF and Δp_T methods, as a function of detector-η for the Jet_20 data (cone size $R = 0.7$). The ratio of $\beta(MPF)$ to $\beta(\Delta p_T)$ is also shown in figure 19. It was found that the correction factor β is different between the MPF and Δp_T methods by approximately 2 % in the region of $1 \lesssim \eta \lesssim 2$ and the difference is larger at higher $|\eta|$'s. Figures 20 and 21 are the same as figure 19 but for the cone sizes of $R = 0.4$ and $R = 1.0$, respectively. The difference between $\beta(MPF)$ and $\beta(\Delta p_T)$ is larger for smaller cone sizes.

3.2.1 For different jet p_T's

Figures 22, 23 and 24 are the same as figures 19-21 but for the Jet_50, Jet_70 and Jet_100 data, respectively. The difference between $\beta(MPF)$ and $\beta(\Delta p_T)$ is smaller at higher jet p_T's; however, $\beta(MPF)$ is always systematically larger than $\beta(\Delta p_T)$ and the difference between $\beta(MPF)$ and $\beta(\Delta p_T)$ is larger for smaller cone sizes.

3.2.2 Dependence on the $\Delta\phi(jet1, 2)$ and $p_T(jet3)$ cuts

Figures 25 and 26 show $\beta(MPF)$ and $\beta(\Delta p_T)$ distributions with and without the $\Delta\phi(jet1, 2) > 2.5$ cut for the Jet_20 data (cone size $R = 0.7$). The differences in both $\beta(MPF)$ and $\beta(\Delta p_T)$ with/without the $\Delta\phi(jet1, 2) > 2.5$ cut are smaller than 1 % for the entire η region.

In figures 27 and 28, $\beta(MPF)$ and $\beta(\Delta p_T)$ distributions without any $p_T(jet3)$ cut and with the $p_T^{jet3} < 8$ and 5 GeV cuts are shown as a function of detector-η. In the region of $|\eta| \lesssim 2.4$, the difference in β due to the change in the the p_T^{jet3} cut is within ~ 1 % for both $\beta(MPF)$ and $\beta(\Delta p_T)$; however, in the region of $|\eta| \gtrsim 2.4$ the change in $\beta(\Delta p_T)$ is larger than that in $\beta(MPF)$.

Figures 29 and 30 are the same as figure 28 but for the cone size $R = 0.4$ and $R = 1.0$, respectively. Similarly to the case of the cone size $R = 0.7$, the difference in β due to the change in the p_T^{jet3} cut is within $1 - 2$ % for both $\beta(MPF)$ and $\beta(\Delta p_T)$ in the region of $|\eta| \lesssim 2.4$, but the difference in $\beta(\Delta p_T)$ becomes larger than that in $\beta(MPF)$ at $|\eta| \gtrsim 2.4$.

We expect that the widths of $\beta(\Delta p_T)$ distributions become larger when the cut on $p_T(jet3)$ is looser because of third jet activities; however, it is not very obvious why the mean $\beta(\Delta p_T)$ values at $|\eta| \gtrsim 2.4$ depend on the $p_T(jet3)$ cut. Although it is beyond the scope of this note to study dijet balancing at $|\eta| \gtrsim 2.4$ in more detail, it might be interesting to address this issue sometime later.

3.2.3 Difference between $\beta(MPF)$ and $\beta(\Delta p_T)$

The bottom plot of figure 31 shows the ratio of $\beta(MPF)/\beta(\Delta p_T)$ as a function of detector-η without any $p_T(jet3)$ cut and with the $p_T(jet3) < 8$ GeV and 5 GeV cuts for the Jet_20 data (cone size $R = 0.7$). When the cut on $p_T(jet3)$ becomes tighter, the difference between $\beta(MPF)$ and $\beta(\Delta p_T)$ at high $|\eta|$'s becomes smaller; however, about 2 % of difference in the region of $1 \lesssim |\eta| \lesssim 2$ (and larger difference at $|\eta| \gtrsim 2$) stays. The difference between $\beta(MPF)$ and $\beta(\Delta p_T)$ at high $|\eta|$'s is larger for the cone size of $R = 0.4$ and smaller for the cone size of $R = 1.0$ as one can see in figures 32 and 33.

One of the possible explanations for this finding is that jets in the forward (plug calorimeter) region have more energy leakage outside the jet cone due to showering in the calorimeter. This is not surprising considering the fact that jets with a fixed $R = \sqrt{\Delta\eta^2 + \Delta\phi^2}$ are smaller in $X - Y$ space at higher $|\eta|$'s as shown in figure 34 and the size of hadron showers (see e.g. Ref. [7][4]). Showering in the calorimeter can cause energy leakage outside the jet cone more easily for jets at higher $|\eta|$'s.

The Δp_T method compares the $\sum E_T$'s inside the cones of the trigger jet and probe jet, while the MPF method utilizes the vector sum of all the calorimeter tower E_T's. It means that the leakage effect is taken into account by the Δp_T method, but not by the MPF method. If forward jets have more leakage outside the jet cone than central jets, $\beta(\Delta p_T)$ should be smaller than $\beta(MPF)$ at high $|\eta|$'s, and forward jet energies corrected by the Δp_T method should be larger than those corrected by the MPF method. To check the conjecture that forward jets have more leakage outside the jet cone than central jets due to showering in the calorimeter, the energy leakage outside the jet cone is studied as a function of η in the next section.

4 Energy leakage outside the jet cone vs detector-η

To check if jets in the forward (plug calorimeter) region have more energy leakage outside the jet cone due to showering in the calorimeter, jet shape observed in the calorimeter is studied as a function of detector-η in this section.

First, we measure the energy density $\rho(r)$ defined as

$$\rho(r) = \frac{\sum E_T(r - \Delta r/2, r + \Delta r/2)}{\sum E_T(0, R)}, \tag{6}$$

where r is a distance from the jet centroid, R is the jet cone radius, and the summations are carried out over all the calorimeter towers within the annuli specified in the parentheses. Please keep in mind that $\rho(r)$ includes the contribution of the energy due to underlying event. Figures 35 and 36 show $\rho(r)$ distributions for each detector-η bin for the Jet_20, 50, 70 and 100 data samples. In these distributions, jets of the cone size $R = 0.4$ are used and $\rho(r)$ is shown over the range of $0 \leq r \leq 1.3$.

[4] In Ref. [7], the width of a shower that contains > 99 % of the visible energy at the shower peak is parametrized by

$$W(E) = -17.28 + 14.28 \ln E(\text{GeV}) \text{ cm},$$

or

$$W(E) = -4.03 + 6.39\sqrt{E(\text{GeV})} \text{ cm}.$$

To evaluate the energy deposited outside the jet cone quantitatively, we form a ratio of the $\sum E_T$ in the annulus of $R \leq r < 1.3$ to that of $r < R$,

$$fOOC = \frac{\sum E_T(R, 1.3)}{\sum E_T(0, R)}. \tag{7}$$

Please note that the sums in both the denominator and numerator of Eq. (7) include the contribution of the underlying event energy and the sum in the numerator is not only due to the energy deposited outside the cone R due to showering. However, assuming that the underlying event energy is flat in η, the variation in $fOOC$ along η indicates the change of the energy leakage outside the jet cone as a function of η.

The value of $fOOC$ of each distribution is shown in each plot in figures 35 and 36. Figures 37 and 38 show $fOOC$ versus detector-η for the cone size $R = 0.4$ for the Jet_20, 50, 70 and 100 data samples. Figures 37 and 38 are the same except for the vertical scale. In figure 37, the vertical scale is fixed to $0.0 - 0.9$ to show the difference between the four data sets; on the other hand, in figure 38 the vertical scale is adjusted for each plot to show the shape of the distribution better. One can see that $fOOC$ is about 3 % larger in the region $1 \lesssim |\eta| \lesssim 2$ than in the central region and becomes even larger at $|\eta| \gtrsim 2$.

Figures 39 and 40 are the same as figure 38 but for the cone size of $R = 0.7$ and $R = 1.0$, respectively. One can see that $fOOC$ is about 2 % larger in the region $1 \lesssim |\eta| \lesssim 2$ than in the central region for the cone size $R = 0.7$, and for the cone size $R = 1.0$ the change in $fOOC$ is within ± 2 %. These findings are consistent with what we expected in section 3.2.3 from the difference between $\beta(MPF)$ and $\beta(\Delta p_T)$.

5 Conclusions

In this note, the relative jet energy corrections obtained from the MPF and Δp_T methods are compared. The corrections obtained from the two methods are found to be different by ~ 2 % in the region of $1 \lesssim \eta \lesssim 2$, which can be explained by the difference between central and plug jets in the energy leakage outside the jet cone due to showering in the calorimeter. The leakage effect is taken into account by the Δp_T method, but not by the MPF method; therefore, the Δp_T method is the more appropriate method to use to obtain the relative jet energy corrections.

References

[1] J-F Auguin *et al.*, Jet Corrections Group, Generic jet energy corrections for Run II data used for the winter conferences, CDF Note 6280.

[2] J-F Auguin *et al.*, Jet Corrections Group, Jet corrections for summer 2003 analyses, CDF Note 6565.

[3] Louis Keeble, New jet correction function QDCSCO version 2.0, CDF Note 1513.

[4] Nathan Eddy, New relative jet corrections for Run 1A and 1B data, CDF Note 3534.

[5] David Brown, A study of dijet p_T matching with 1987 data, CDF Note 835.

[6] Good run list page,
http://www-cdf.fnal.gov/internal/dqm/goodrun/good.html

[7] A. L. Sessoms *et al.*, The segmented calorimeter: a study of hadron shower structure, *Nucl. Instrum. Meth.* **161** (1979) 371.

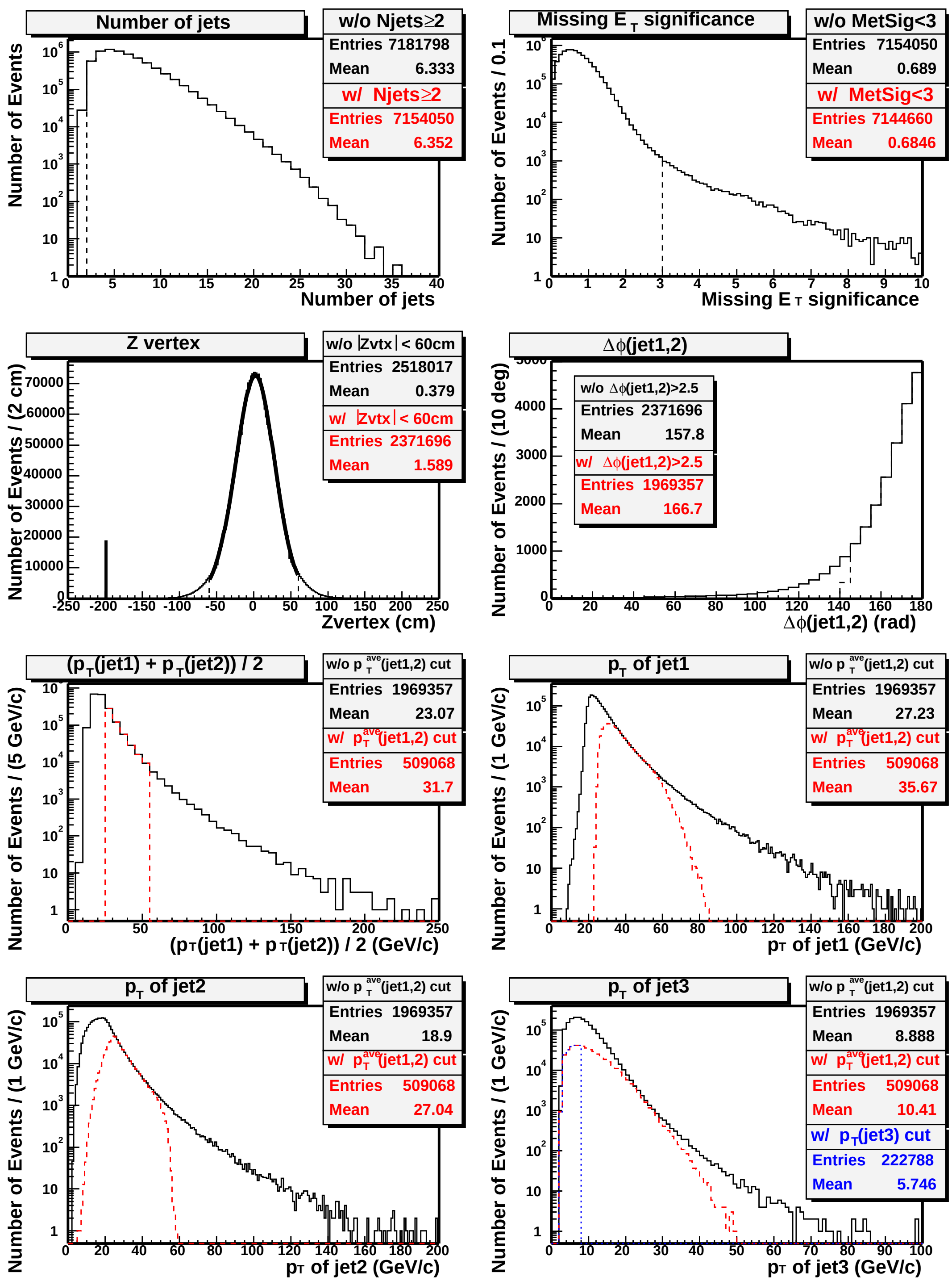

Figure 2: Distributions of number of jets, missing E_T significance, z_{vertex}, the azimuthal angle between the leading two jets $\Delta\phi(jet1, 2)$, the average p_T of the leading two jets $p_T^{ave}(jet1, 2)$, p_T of the leading three jets, before and after each event selection cut for the Jet_20 data sample.

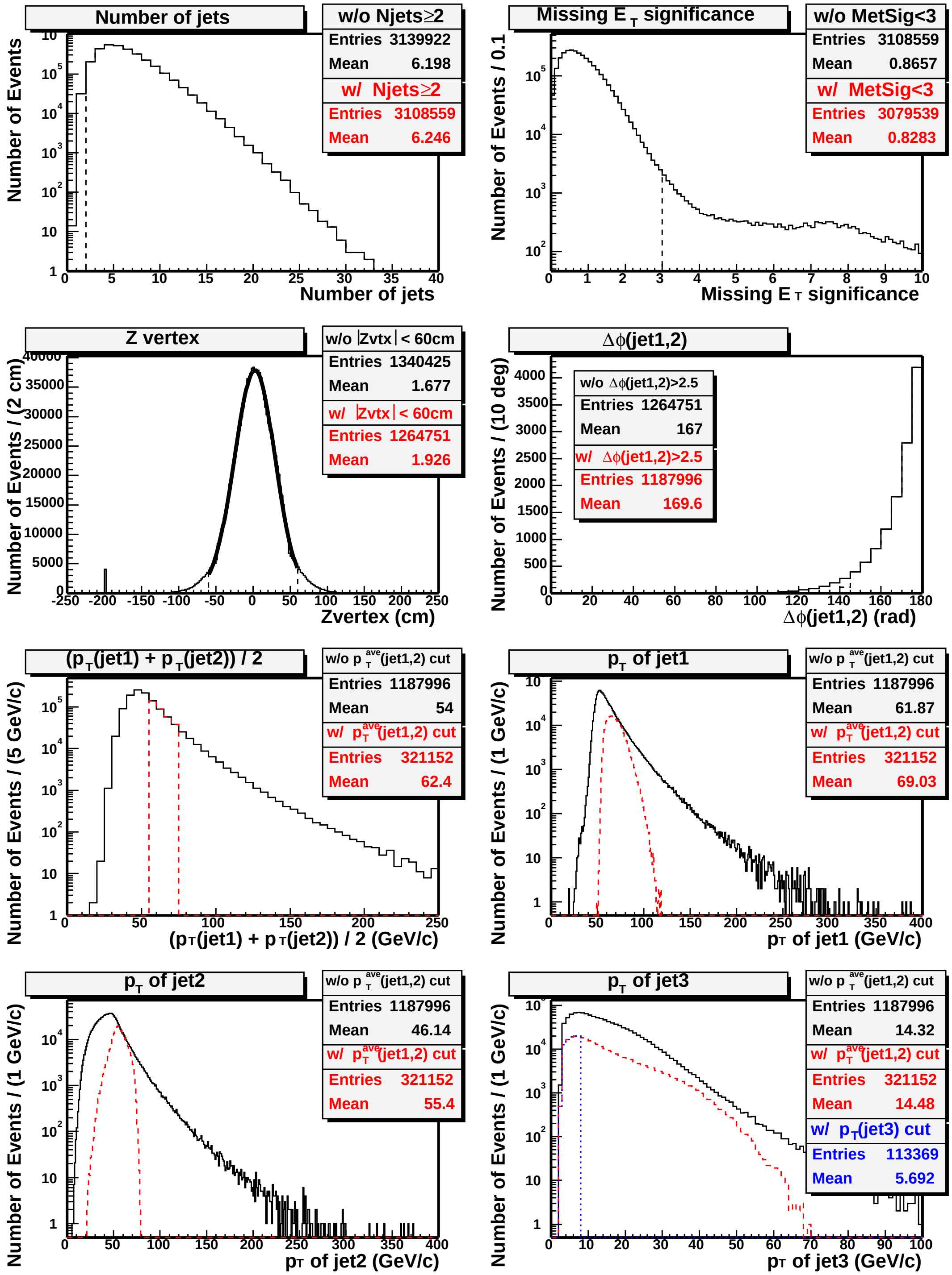

Figure 3: Distributions of number of jets, missing E_T significance, z_{vertex}, the azimuthal angle between the leading two jets $\Delta\phi(jet1,2)$, the average p_T of the leading two jets $p_T^{ave}(jet1,2)$, p_T of the leading three jets, before and after each event selection cut for the Jet_50 data sample.

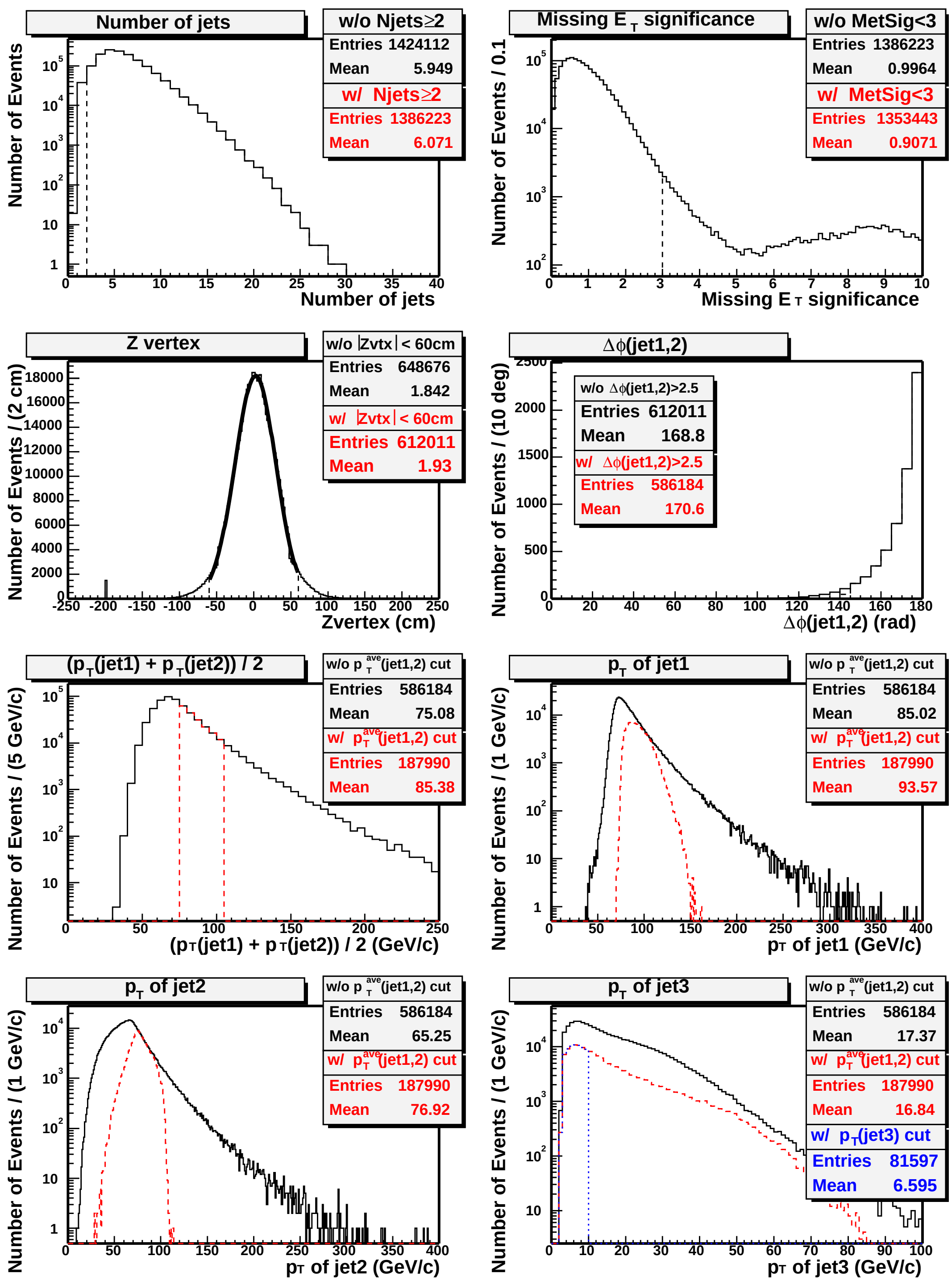

Figure 4: Distributions of number of jets, missing E_T significance, z_{vertex}, the azimuthal angle between the leading two jets $\Delta\phi(jet1,2)$, the average p_T of the leading two jets $p_T^{ave}(jet1,2)$, p_T of the leading three jets, before and after each event selection cut for the Jet_70 data sample.

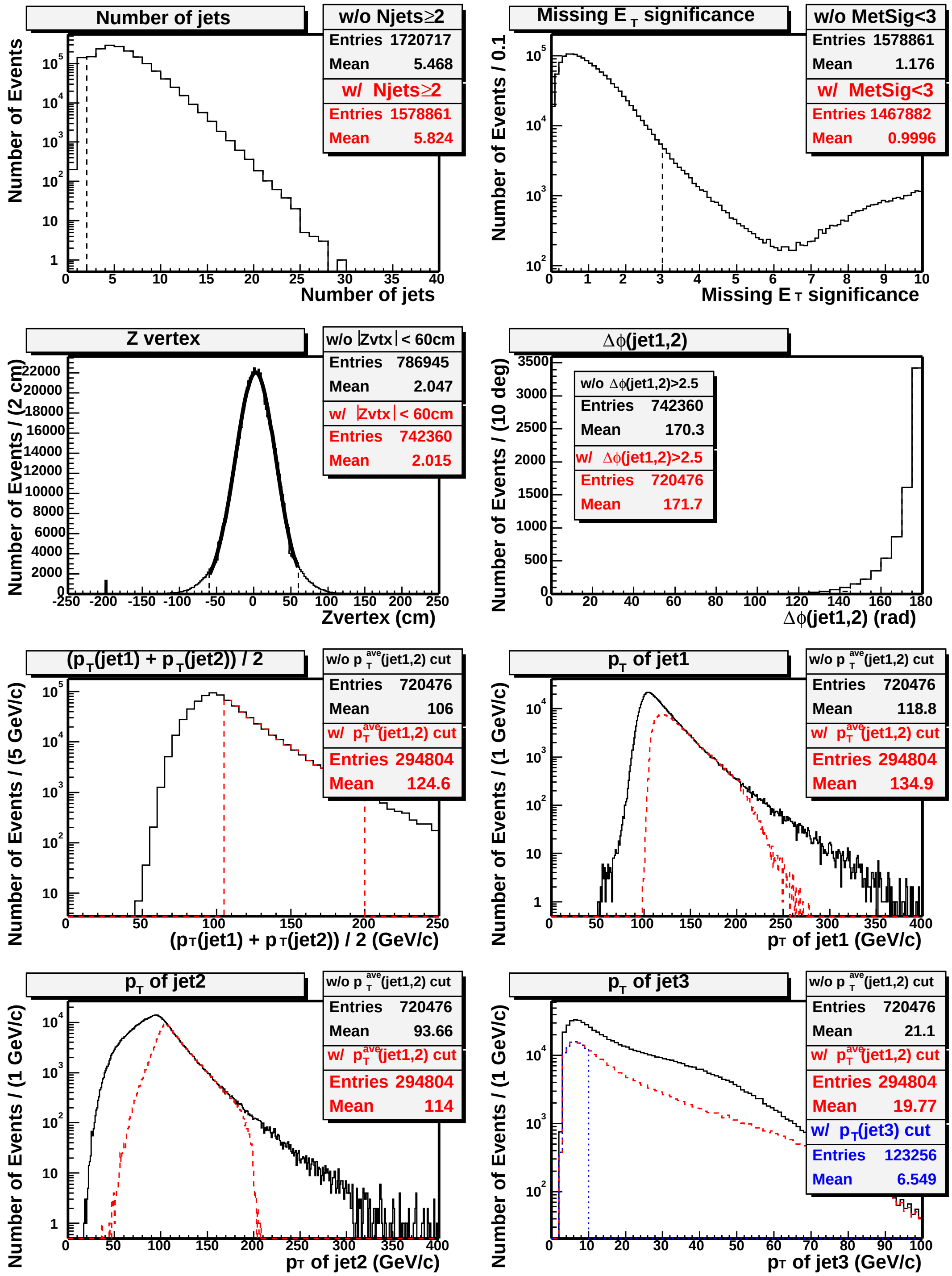

Figure 5: Distributions of number of jets, missing E_T significance, z_{vertex}, the azimuthal angle between the leading two jets $\Delta\phi(jet1,2)$, the average p_T of the leading two jets $p_T^{ave}(jet1,2)$, p_T of the leading three jets, before and after each event selection cut for the Jet_100 data sample.

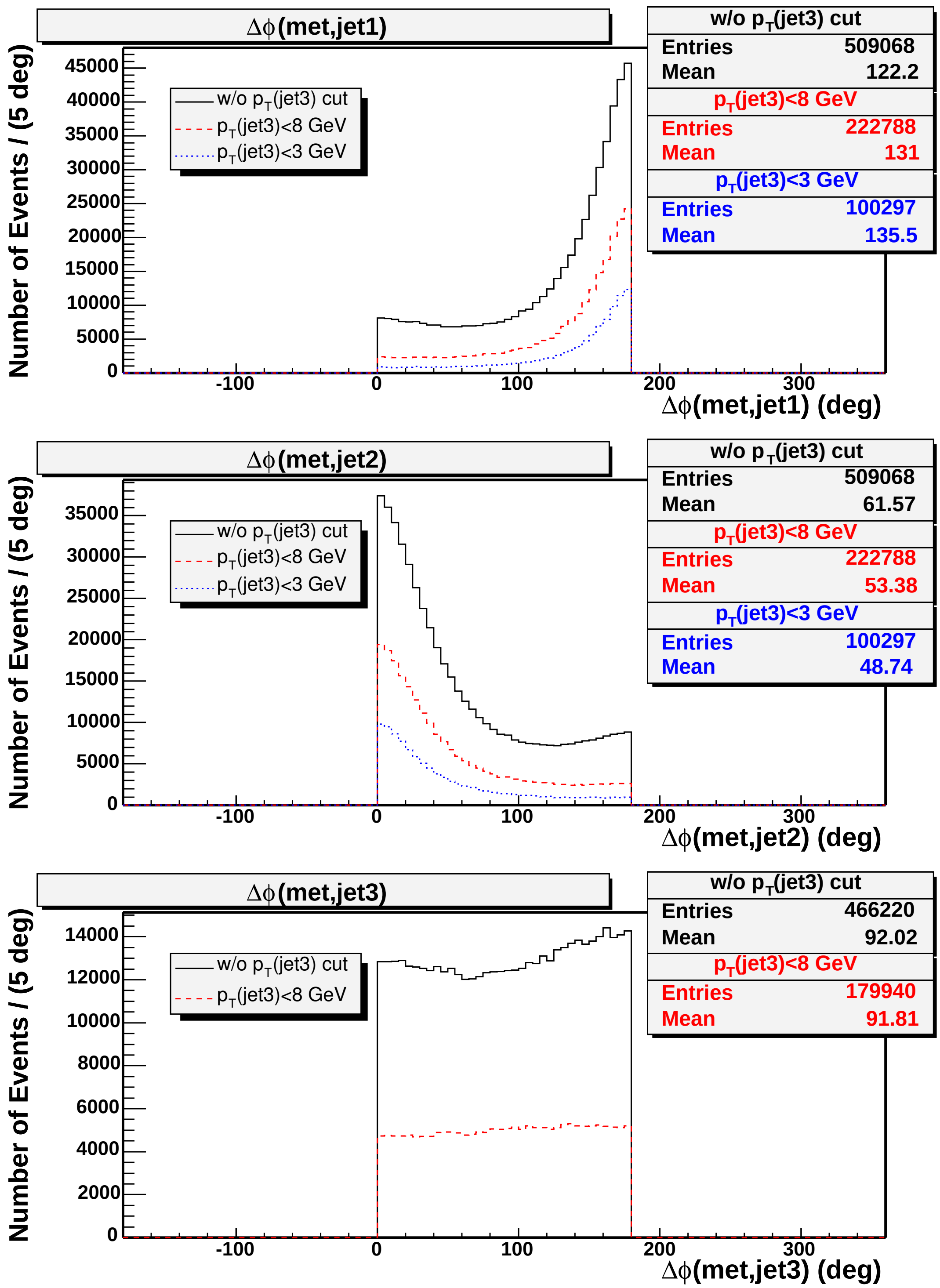

Figure 6: Distributions of $\Delta\phi$ between the missing E_T and the leading three jets (cone size $R = 0.7$) with the different cuts on $p_T(jet3)$ for the Jet_20 data.

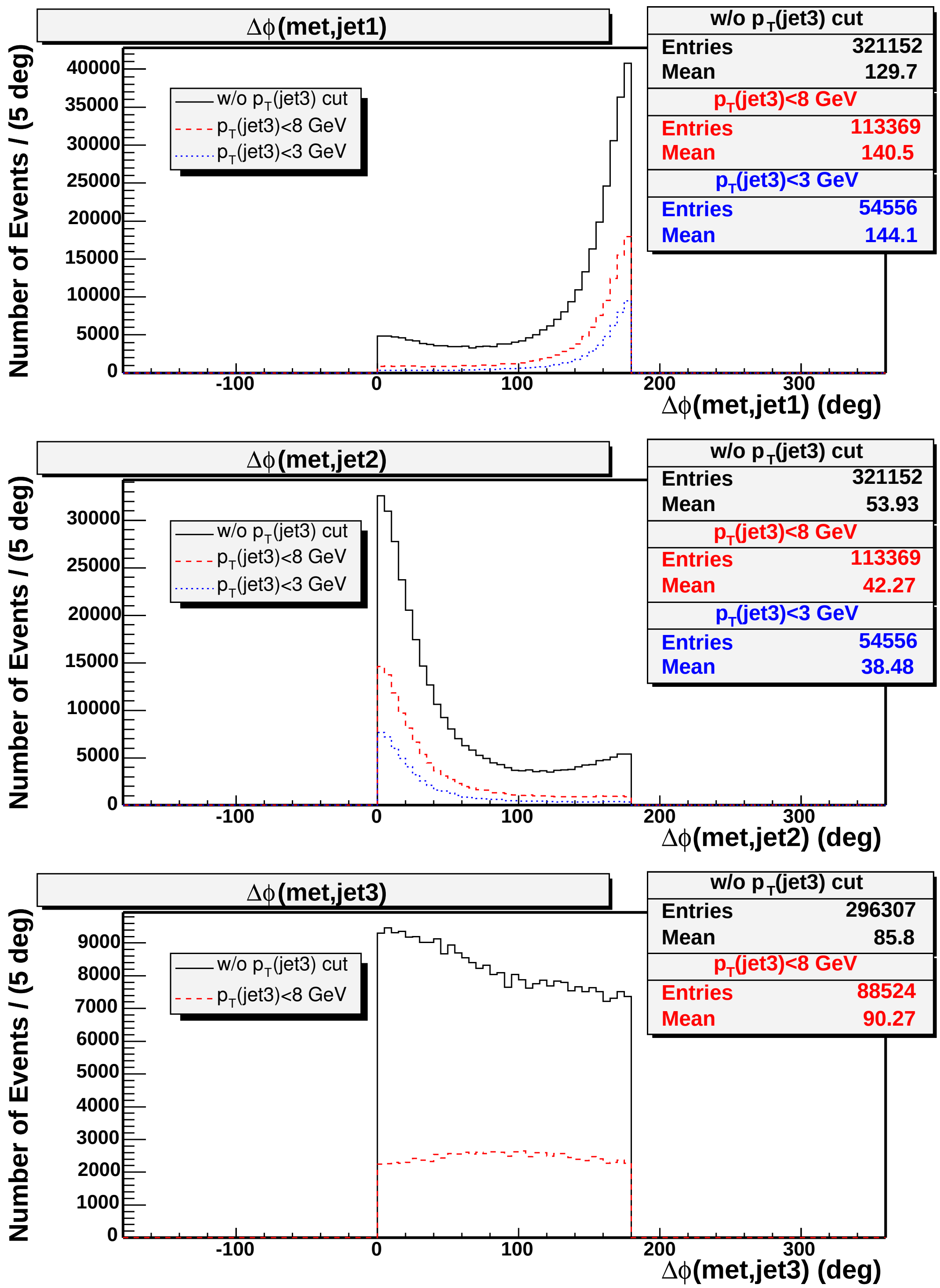

Figure 7: Distributions of $\Delta\phi$ between the missing E_T and the leading three jets (cone size $R = 0.7$) with the different cuts on $p_T(jet3)$ for the Jet_50 data.

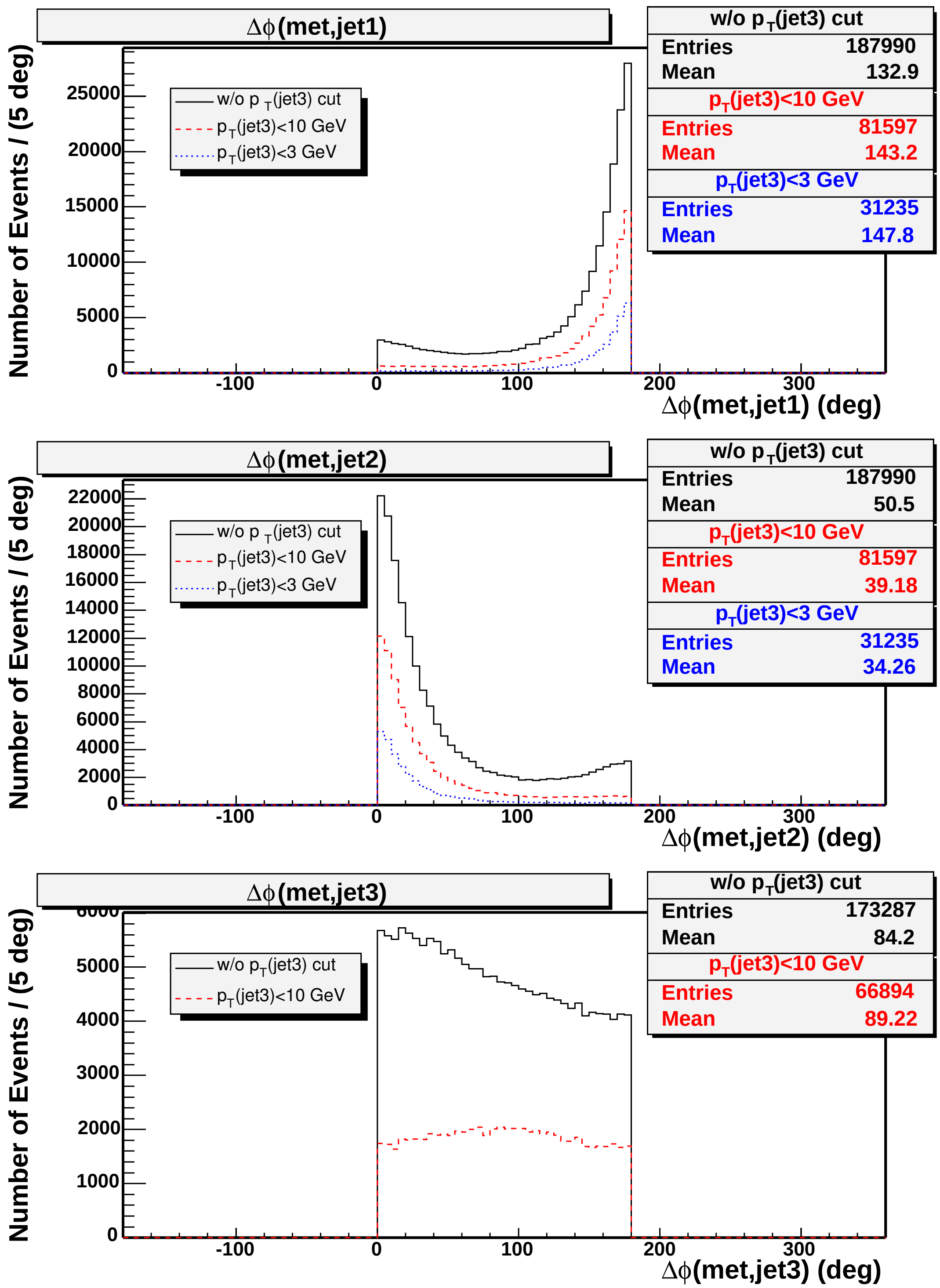

Figure 8: Distributions of $\Delta\phi$ between the missing E_T and the leading three jets (cone size $R = 0.7$) with the different cuts on $p_T(jet3)$ for the Jet_70 data.

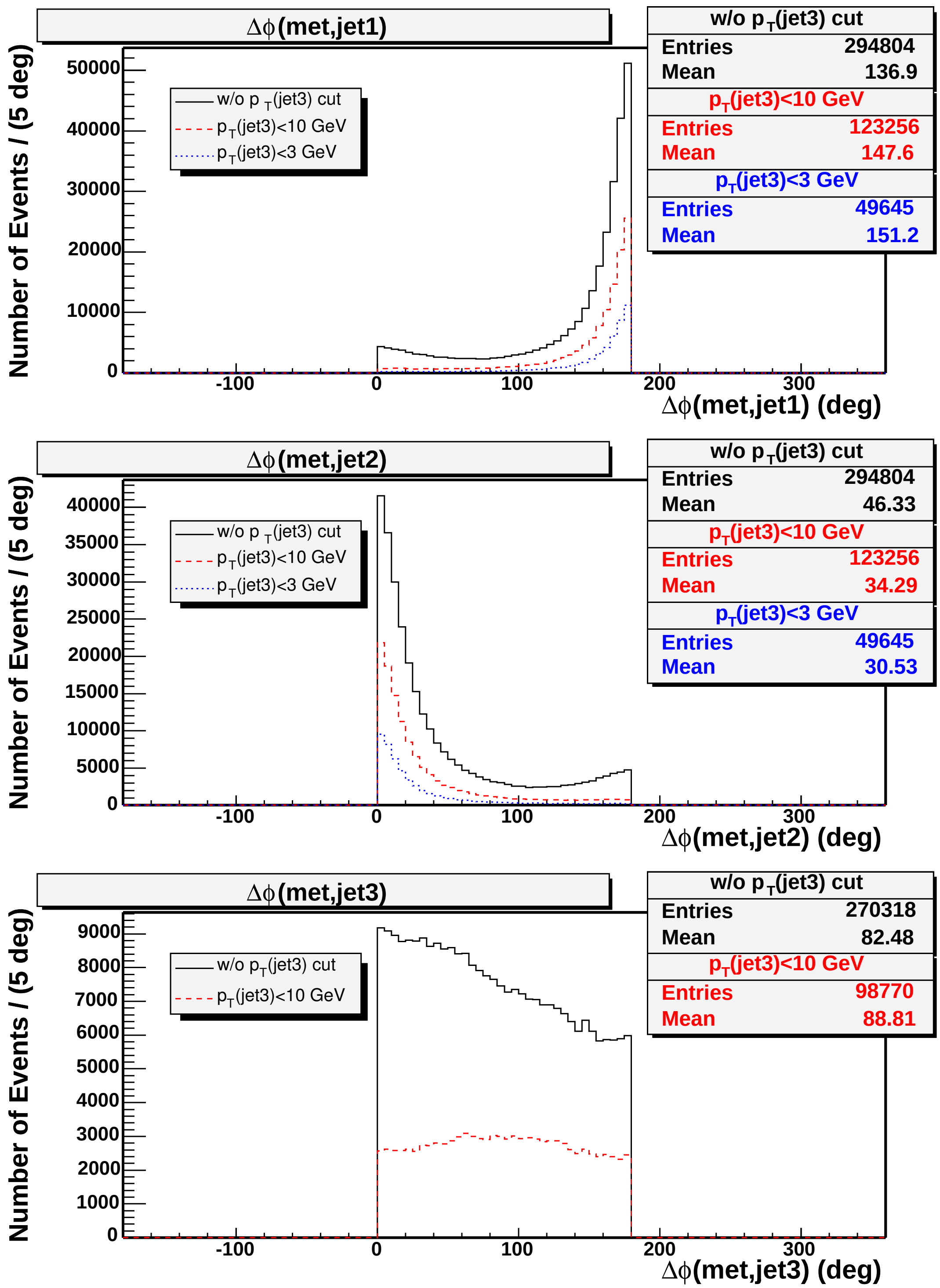

Figure 9: Distributions of $\Delta\phi$ between the missing E_T and the leading three jets (cone size $R = 0.7$) with the different cuts on $p_T(jet3)$ for the Jet_100 data.

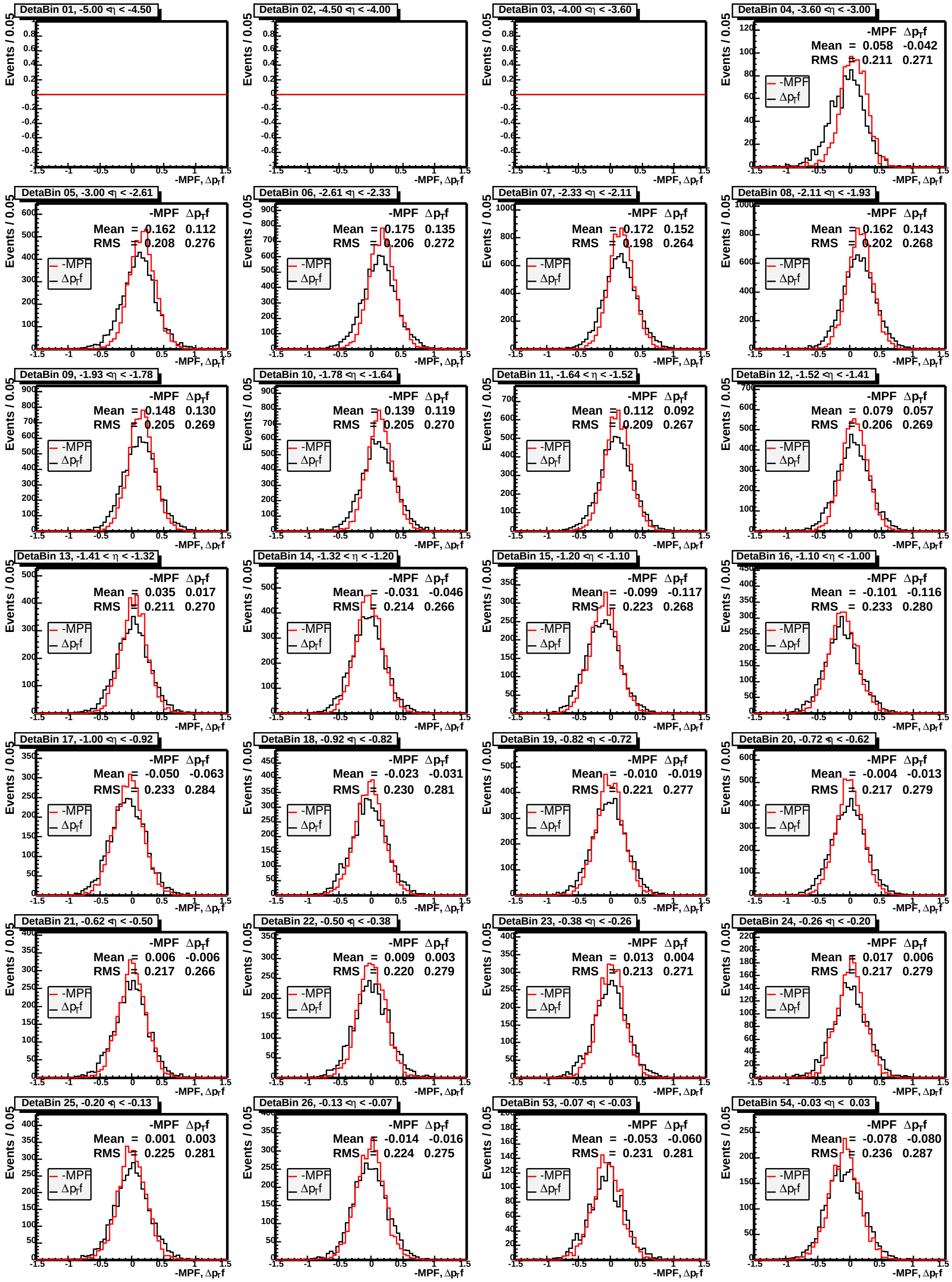

Figure 10: Distributions of $-\mathrm{MPF}$ and $\Delta p_T f$ in detector-η bins on the negative η side for the Jet_20 data (cone size $R = 0.7$).

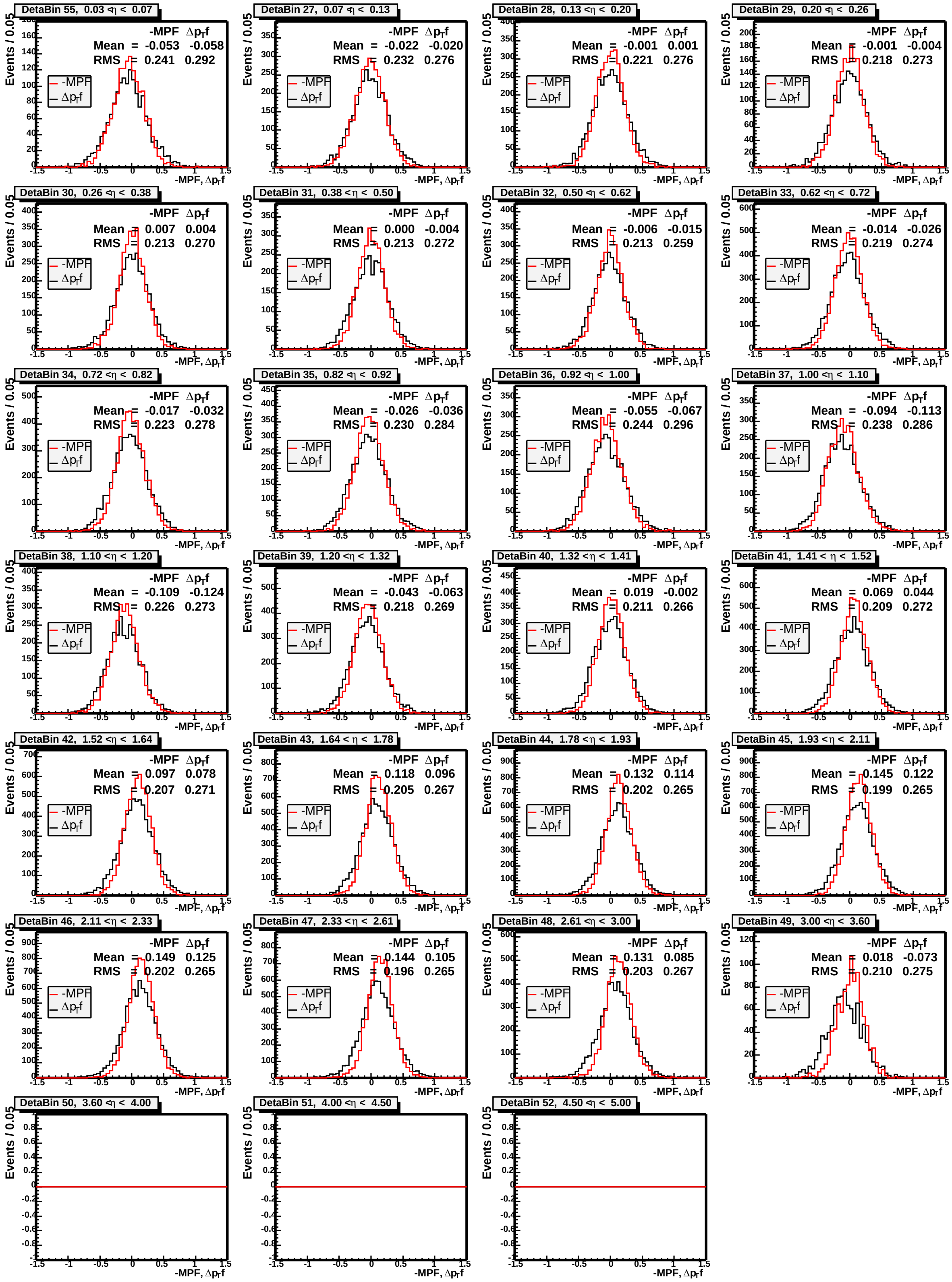

Figure 11: Distributions of $-\mathrm{MPF}$ and $\Delta p_T f$ in detector-η bins on the positive η side for the Jet_20 data (cone size $R = 0.7$).

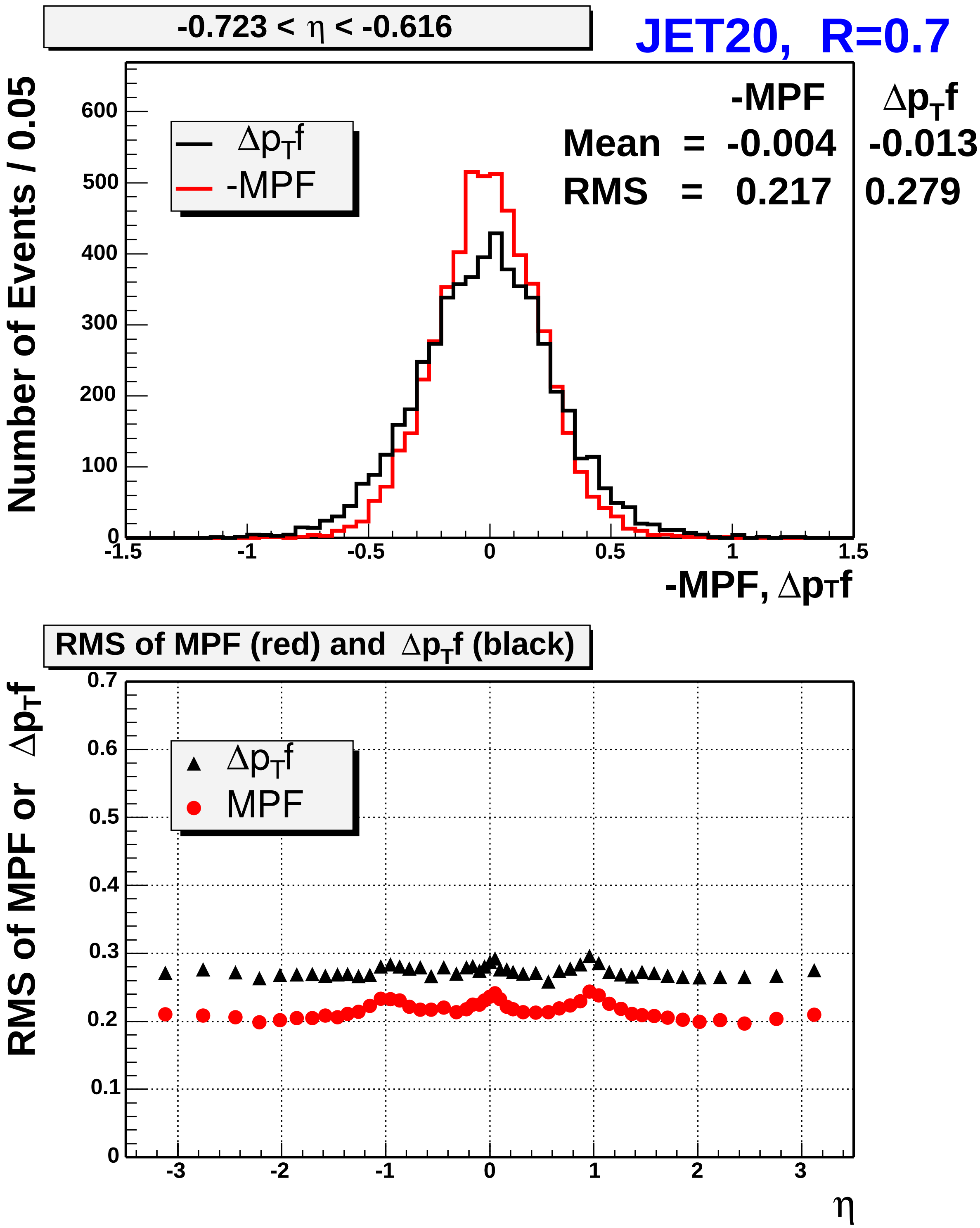

Figure 12: (top) Distributions of $-\mathrm{MPF}$ and $\Delta p_T f$ in the detector-η bin of $-0.723 < \eta < -0.616$ for the Jet_20 data (cone size $R = 0.7$). (bottom) The RMS of the MPF and $\Delta p_T f$ distributions as a function of detector-η.

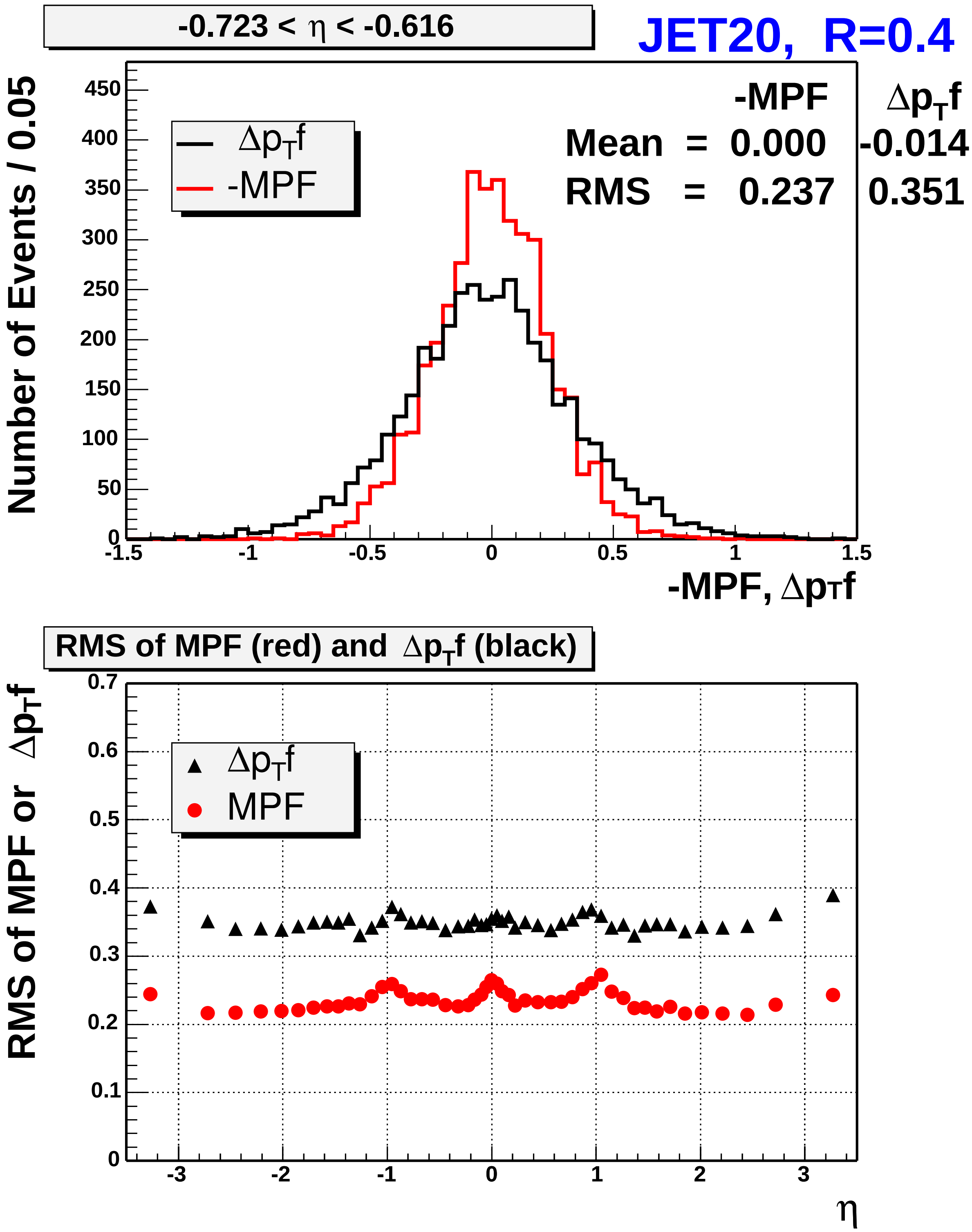

Figure 13: (top) Distributions of $-$MPF and $\Delta p_T f$ in the detector-η bin of $-0.723 < \eta < -0.616$ for the Jet_20 data (cone size $R = 0.4$). (bottom) The RMS of the MPF and $\Delta p_T f$ distributions as a function of detector-η.

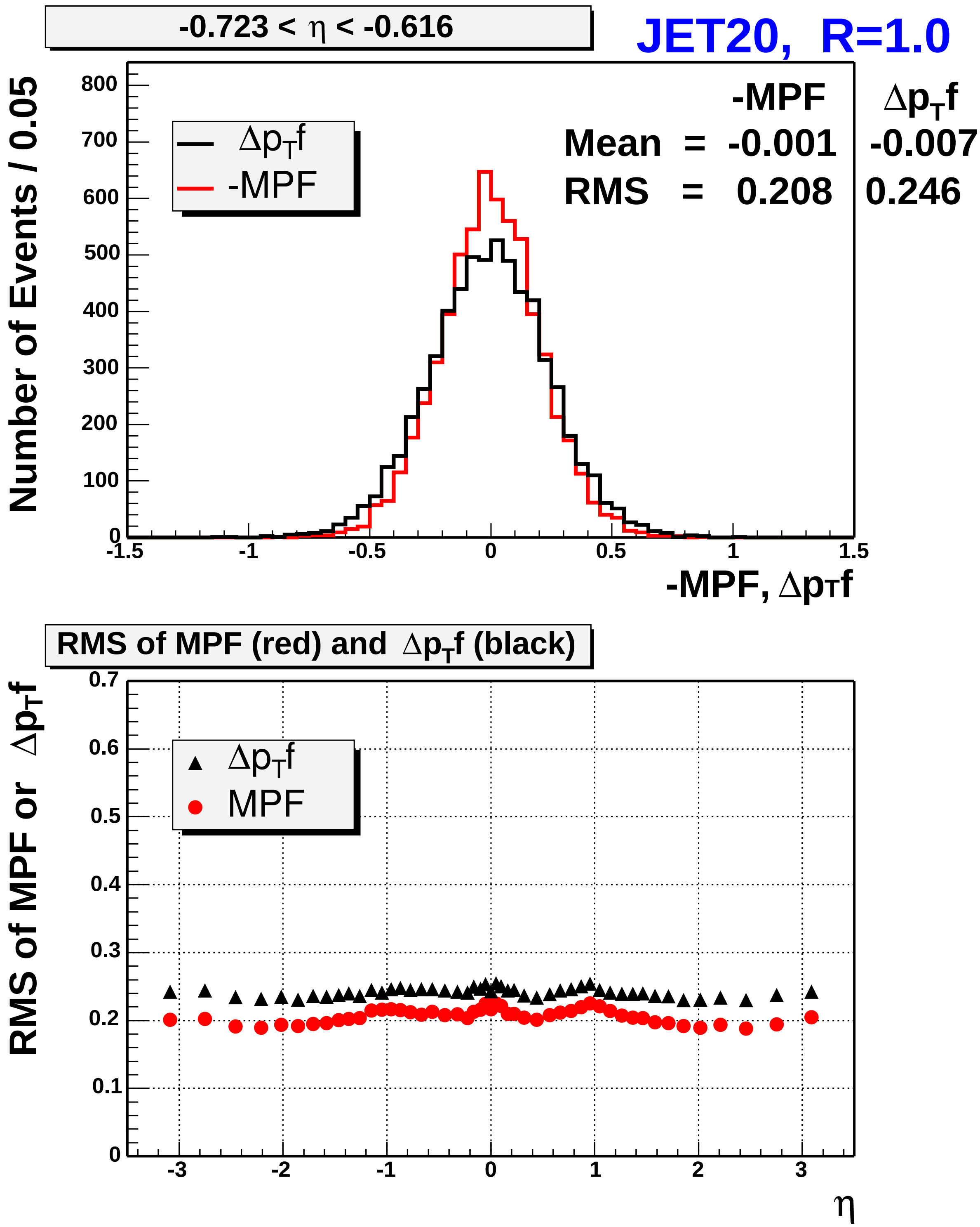

Figure 14: (top) Distributions of $-\text{MPF}$ and $\Delta p_T f$ in the detector-η bin of $-0.723 < \eta < -0.616$ for the Jet_20 data (cone size $R = 1.0$). (bottom) The RMS of the MPF and $\Delta p_T f$ distributions as a function of detector-η.

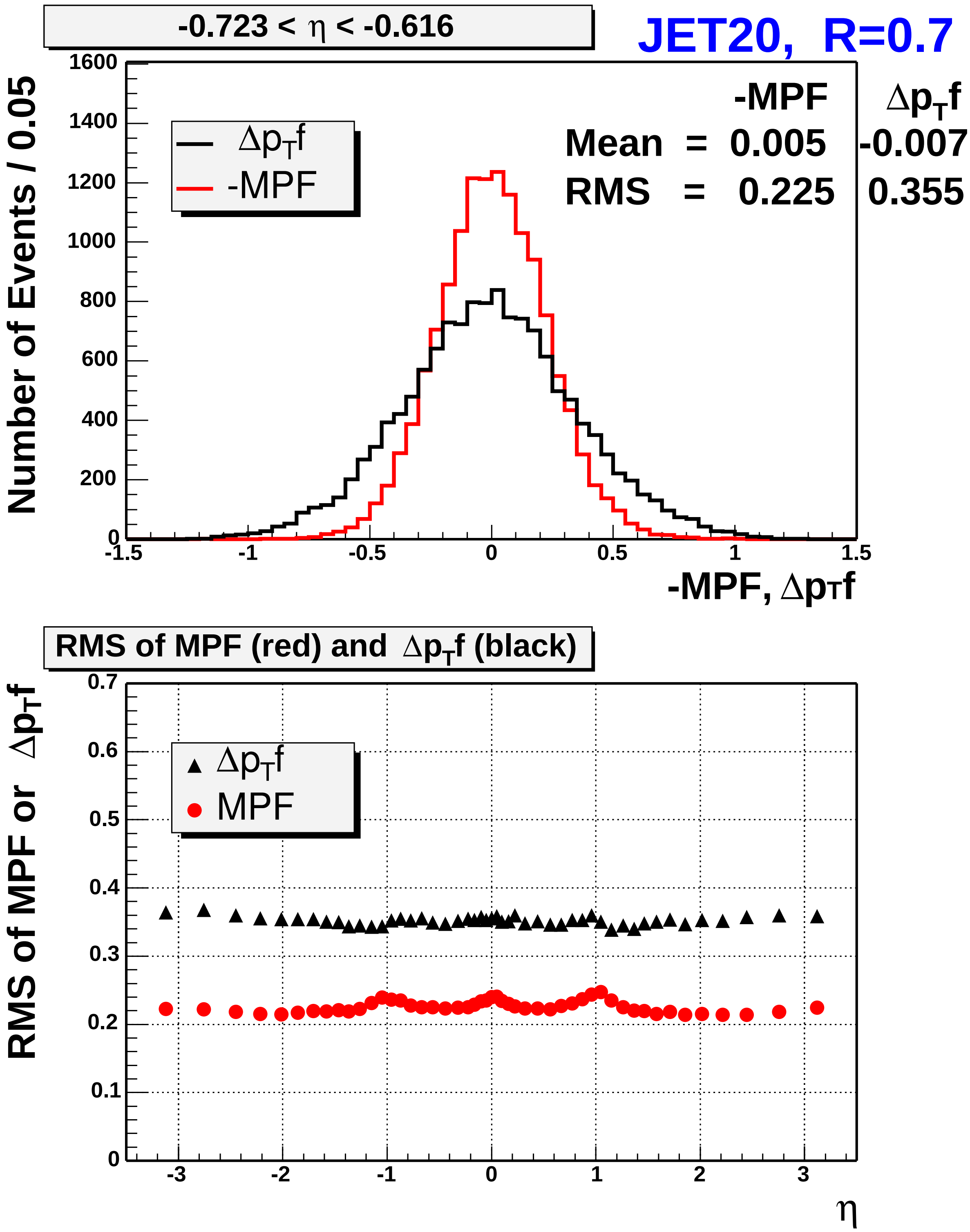

Figure 15: (top) Distributions of $-$MPF and $\Delta p_T f$ in the detector-η bin of $-0.723 < \eta < -0.616$ for the Jet_20 data (cone size $R = 1.0$). (bottom) The RMS of the MPF and $\Delta p_T f$ distributions as a function of detector-η.

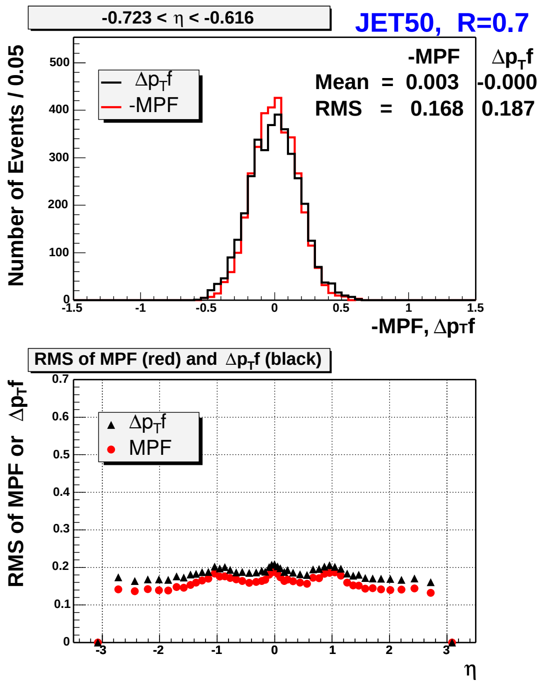

(a) Cone size $R = 0.7$

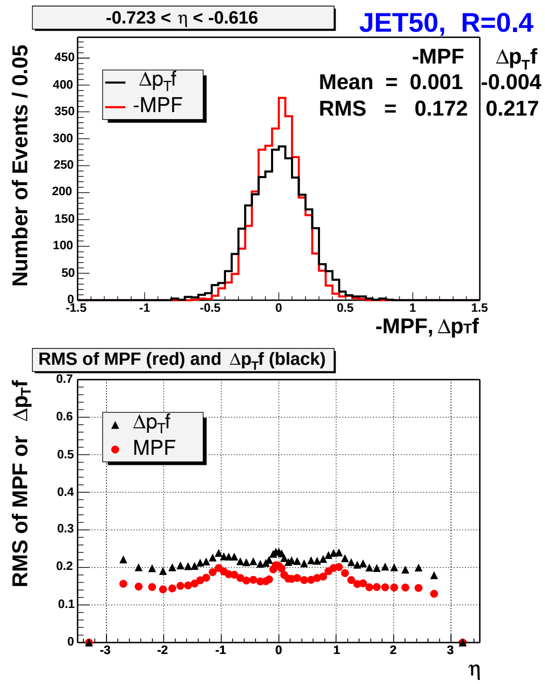

(b) Cone size $R = 0.4$

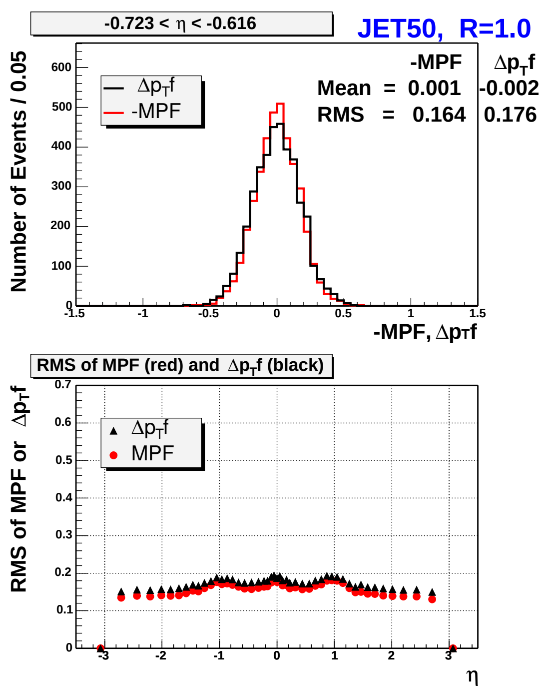

(c) Cone size $R = 1.0$

Figure 16: (top) Distributions of $-$MPF and $\Delta p_T f$ in the detector-η bin of $-0.723 < \eta < -0.616$, and (bottom) the RMS of the MPF and $\Delta p_T f$ distributions as a function of detector-η for the Jet_50 data for the cone sizes of $R = 0.7$ (a), 0.4 (b) and 1.0 (c).

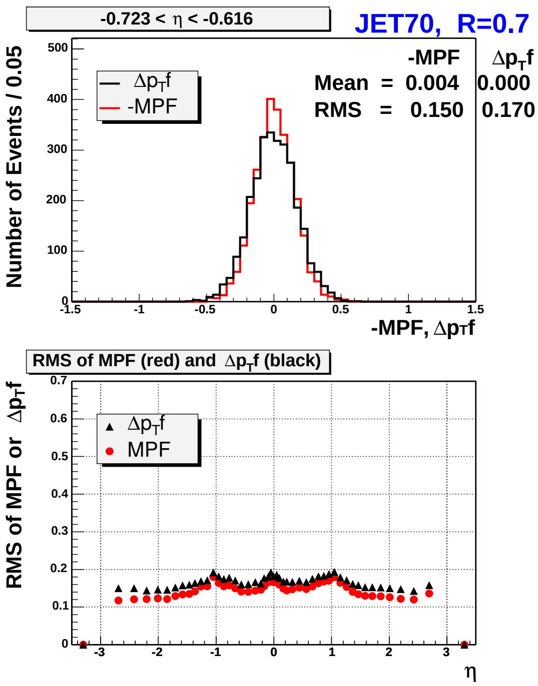

(a) Cone size $R = 0.7$

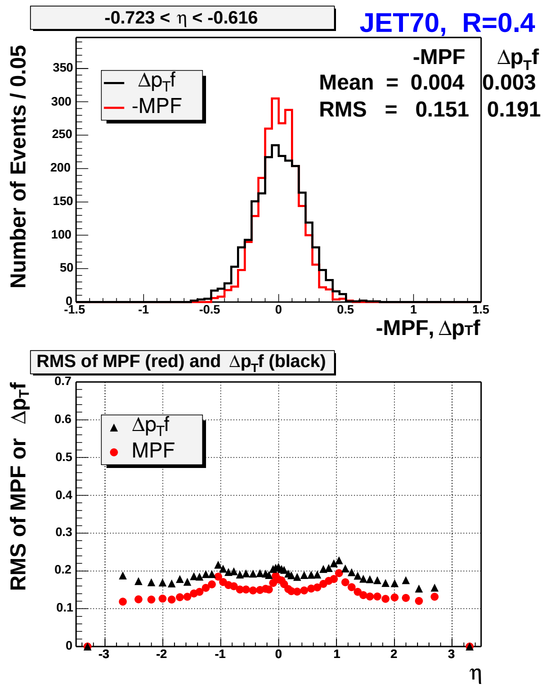

(b) Cone size $R = 0.4$

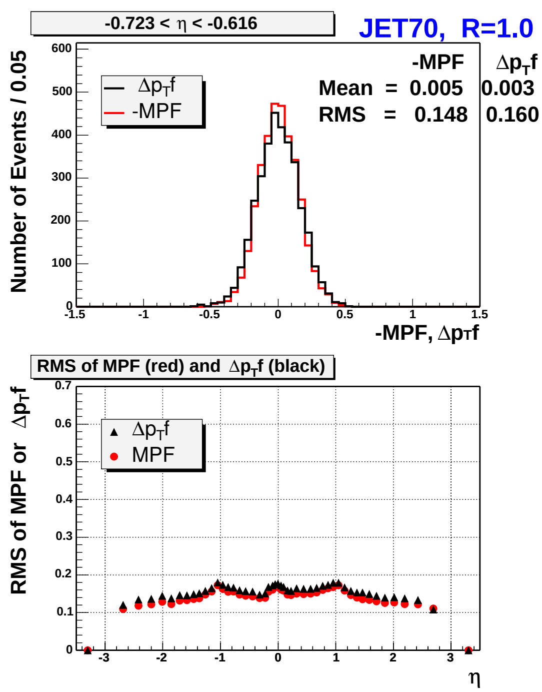

(c) Cone size $R = 1.0$

Figure 17: (top) Distributions of $-$MPF and $\Delta p_T f$ in the detector-η bin of $-0.723 < \eta < -0.616$, and (bottom) the RMS of the MPF and $\Delta p_T f$ distributions as a function of detector-η for the Jet_70 data for the cone sizes of $R = 0.7$ (a), 0.4 (b) and 1.0 (c).

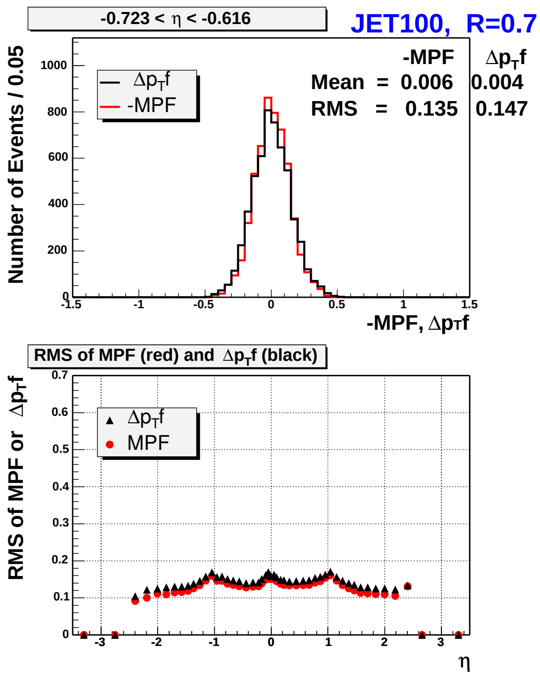

(a) Cone size $R = 0.7$

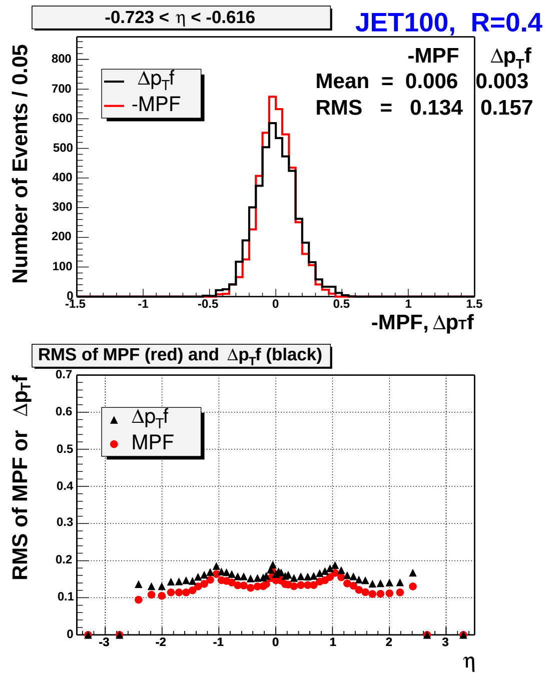

(b) Cone size $R = 0.4$

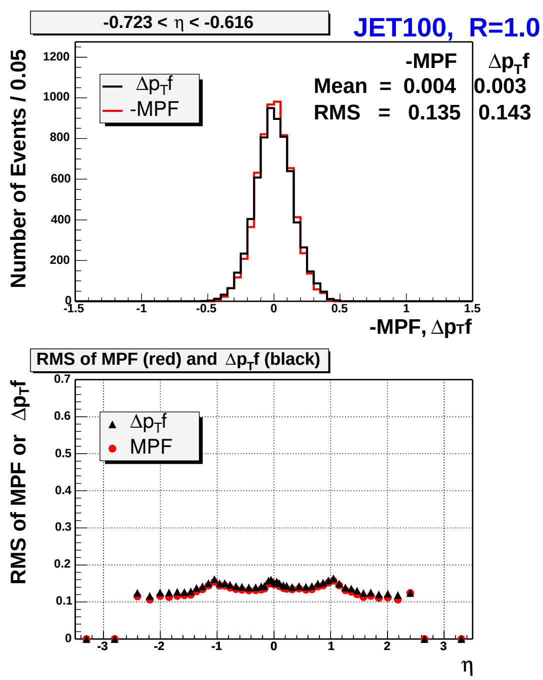

(c) Cone size $R = 1.0$

Figure 18: (top) Distributions of $-$MPF and $\Delta p_T f$ in the detector-η bin of $-0.723 < \eta < -0.616$, and (bottom) the RMS of the MPF and $\Delta p_T f$ distributions as a function of detector-η for the Jet_100 data for the cone sizes of $R = 0.7$ (a), 0.4 (b) and 1.0 (c).

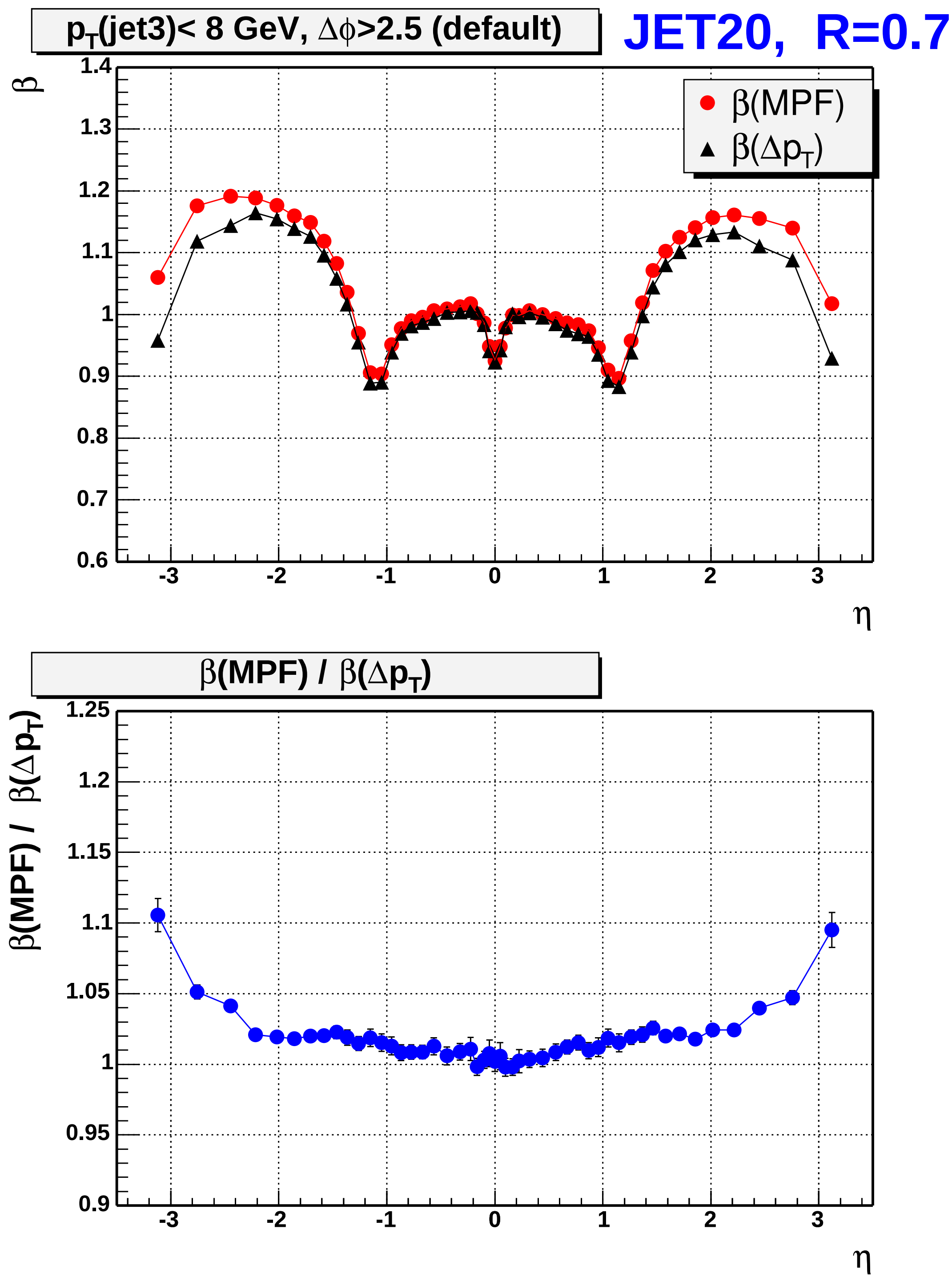

Figure 19: (top) The correction factors $\beta(MPF)$ (red circles) and $\beta(\Delta p_T)$ (black triangles) from the MPF and Δp_T methods as a function of detector-η, and (bottom) the ratio of $\beta(MPF)$ to $\beta(\Delta p_T)$ as a function of detector-η for the Jet_20 data (cone size $R = 0.7$).

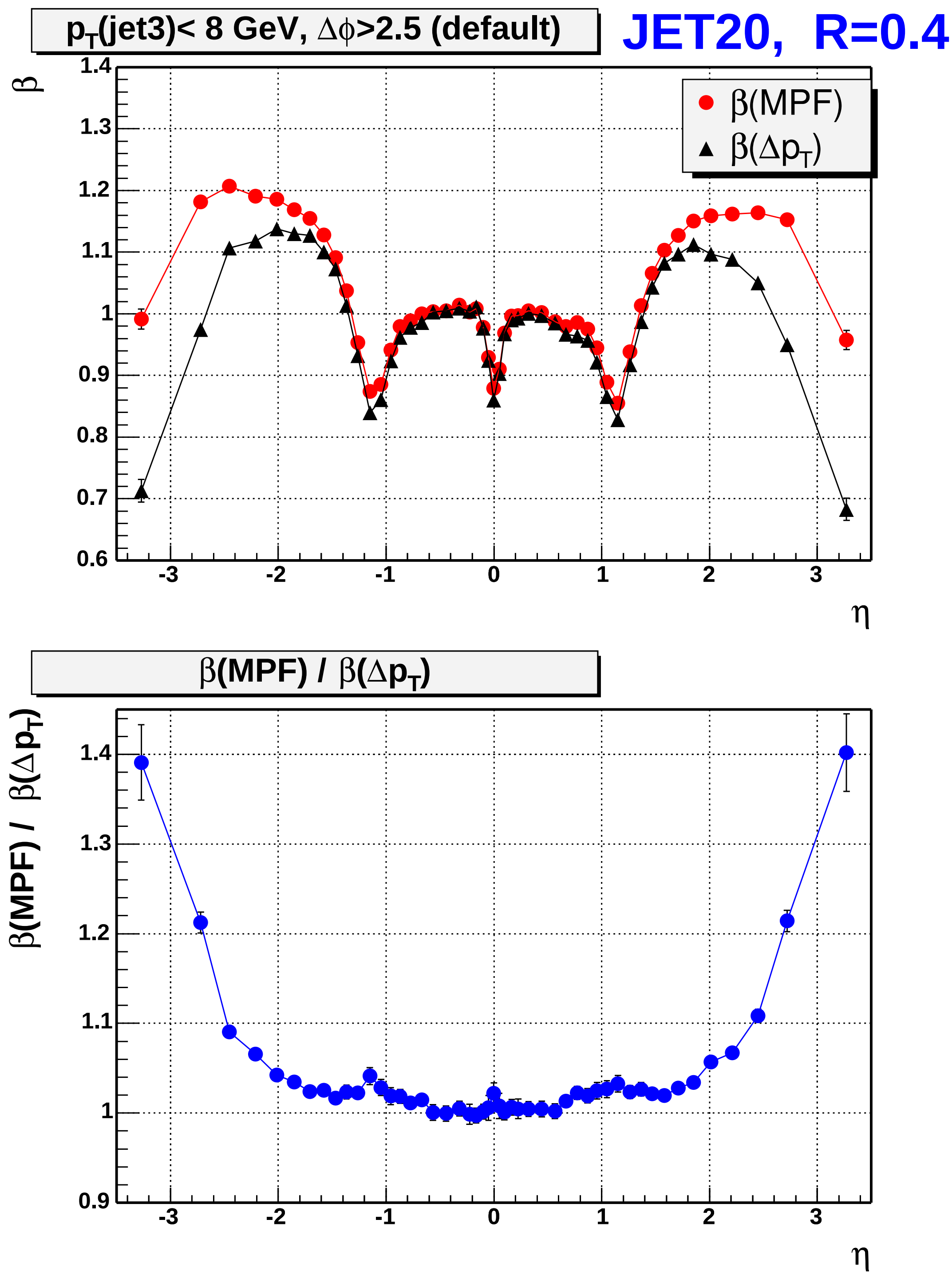

Figure 20: (top) The correction factors $\beta(MPF)$ (red circles) and $\beta(\Delta p_T)$ (black triangles) from the MPF and Δp_T methods as a function of detector-η, and (bottom) the ratio of $\beta(MPF)$ to $\beta(\Delta p_T)$ as a function of detector-η for the Jet_20 data (cone size $R = 0.4$).

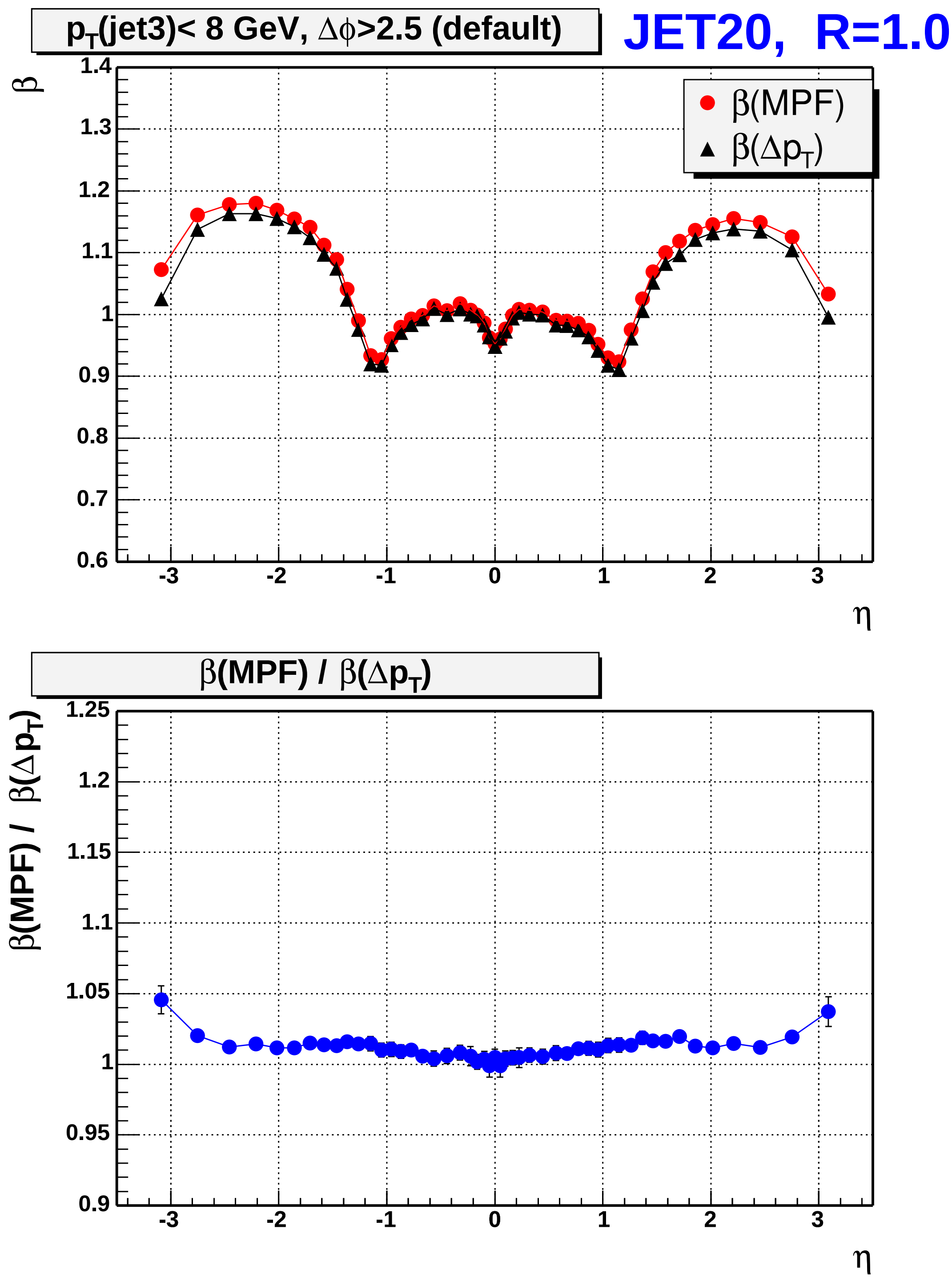

Figure 21: (top) The correction factors $\beta(MPF)$ (red circles) and $\beta(\Delta p_T)$ (black triangles) from the MPF and Δp_T methods as a function of detector-η, and (bottom) the ratio of $\beta(MPF)$ to $\beta(\Delta p_T)$ as a function of detector-η for the Jet_20 data (cone size $R = 1.0$).

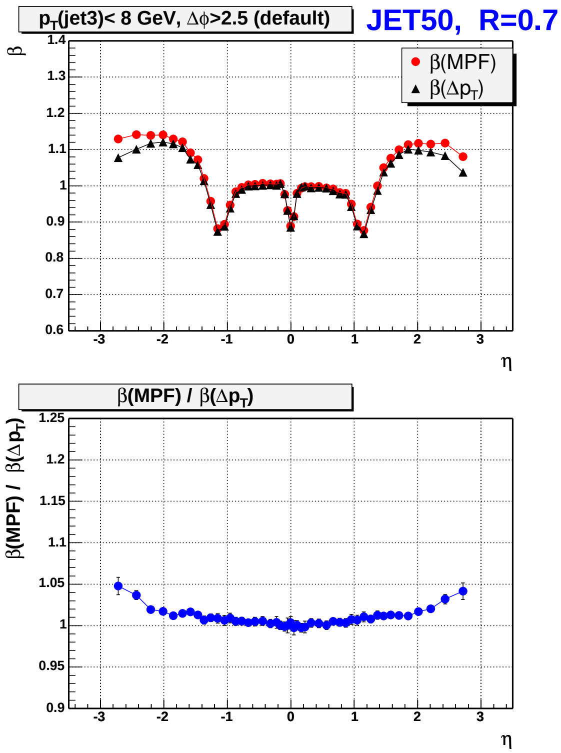

(a) $R = 0.7$

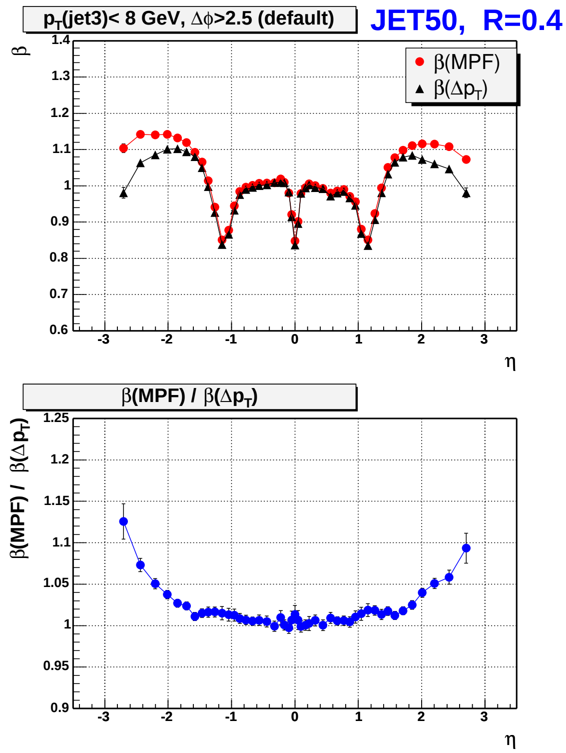

(b) $R = 0.4$

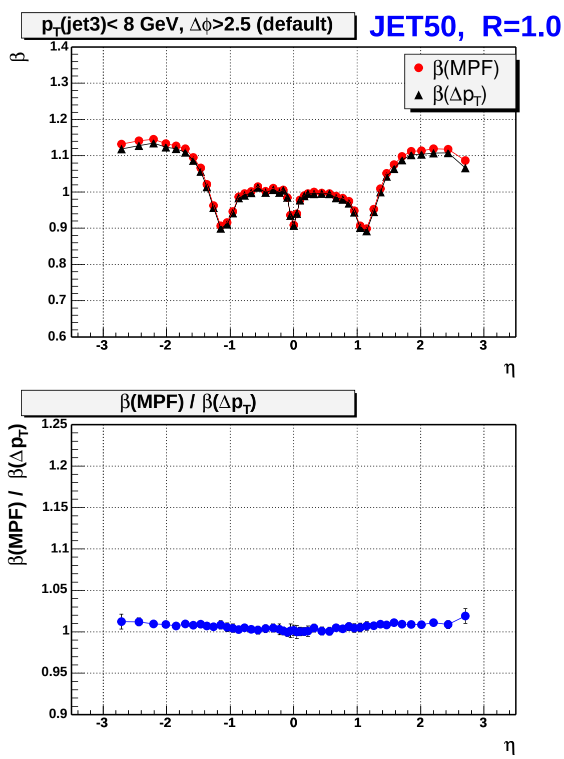

(c) $R = 1.0$

Figure 22: (top) The correction factors $\beta(MPF)$ (red circles) and $\beta(\Delta p_T)$ (black triangles) from the MPF and Δp_T methods as a function of detector-η, and (bottom) the ratio of $\beta(MPF)$ to $\beta(\Delta p_T)$ as a function of detector-η for the Jet_50 data.

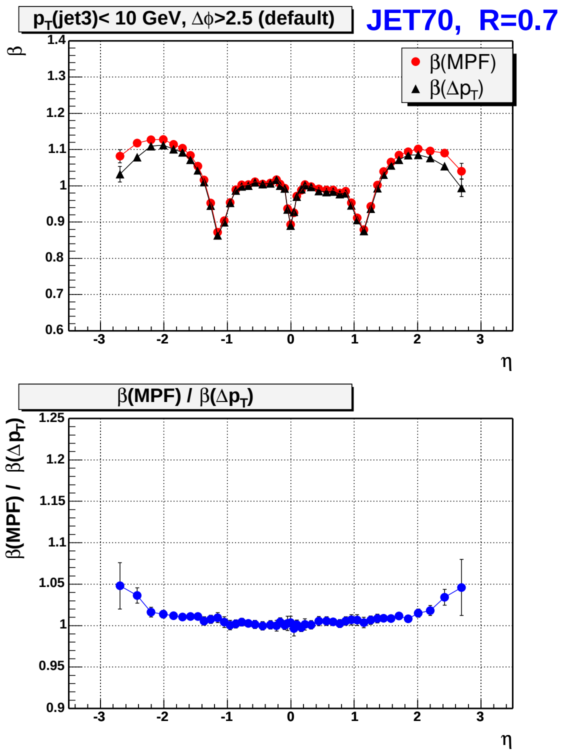

(a) $R = 0.7$

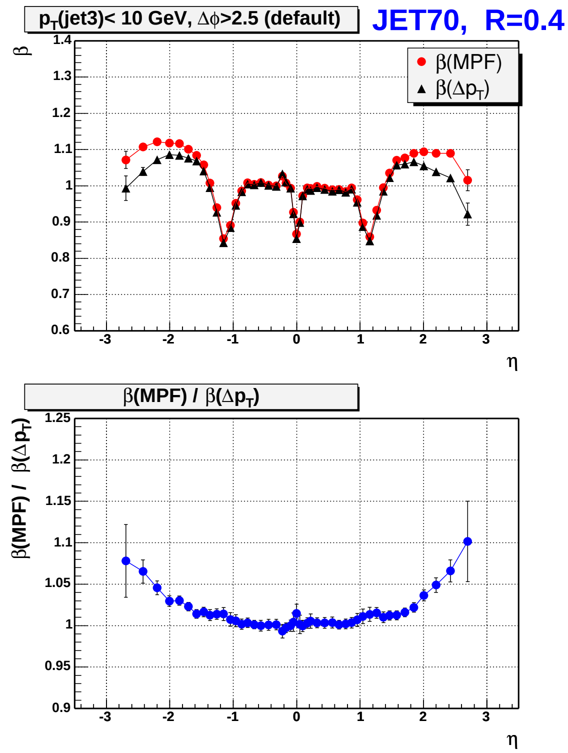

(b) $R = 0.4$

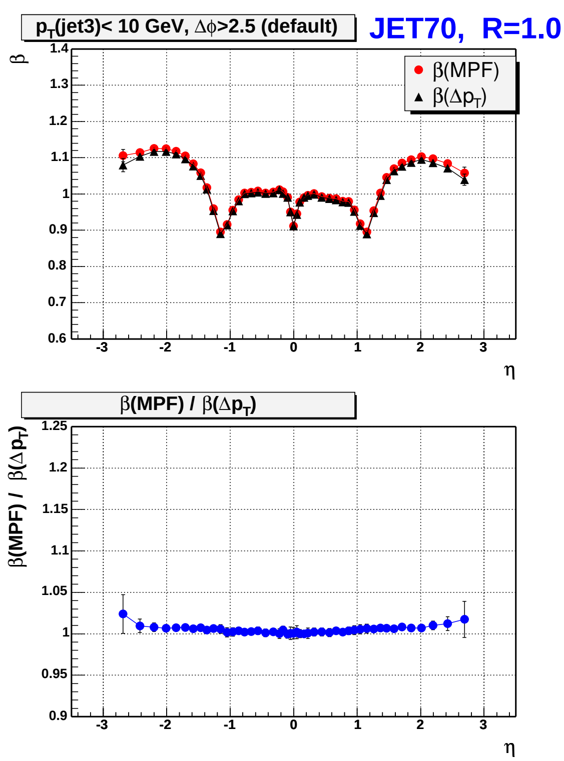

(c) $R = 1.0$

Figure 23: (top) The correction factors $\beta(MPF)$ (red circles) and $\beta(\Delta p_T)$ (black triangles) from the MPF and Δp_T methods as a function of detector-η, and (bottom) the ratio of $\beta(MPF)$ to $\beta(\Delta p_T)$ as a function of detector-η for the Jet_70 data.

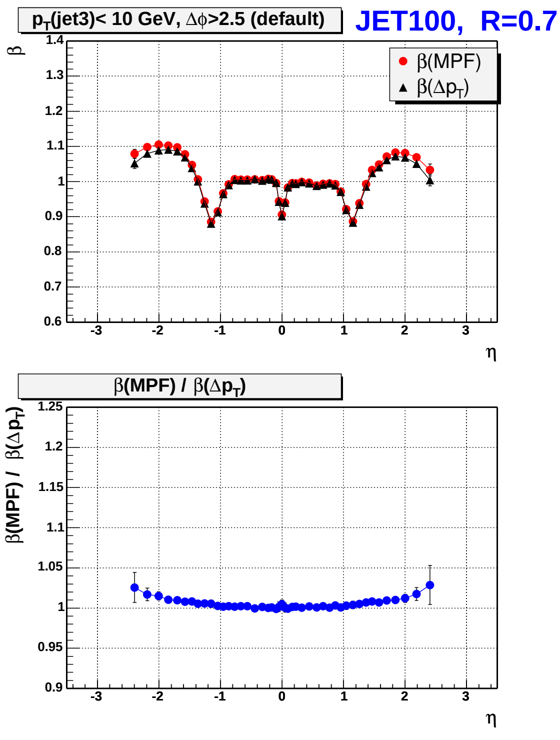

(a) $R = 0.7$

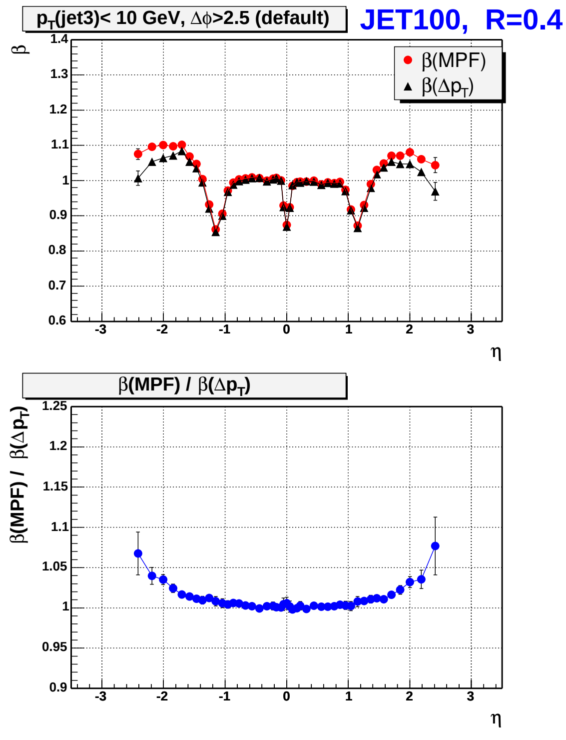

(b) $R = 0.4$

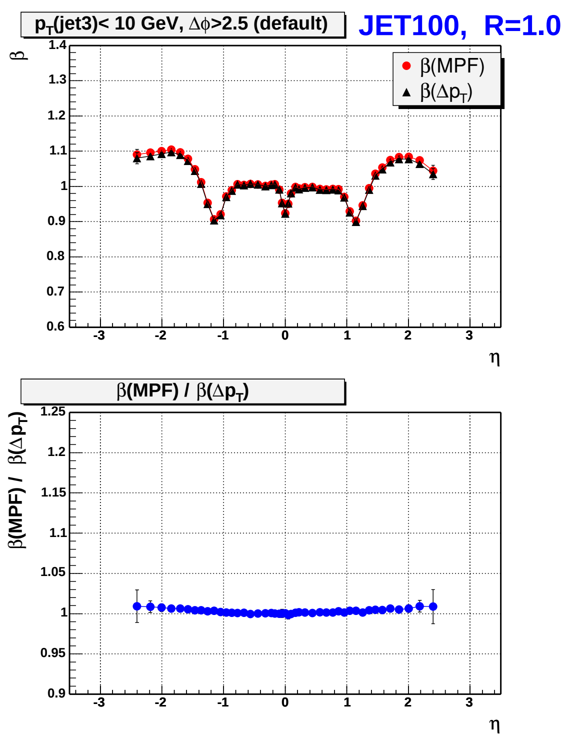

(c) $R = 1.0$

Figure 24: (top) The correction factors $\beta(MPF)$ (red circles) and $\beta(\Delta p_T)$ (black triangles) from the MPF and Δp_T methods as a function of detector-η, and (bottom) the ratio of $\beta(MPF)$ to $\beta(\Delta p_T)$ as a function of detector-η for the Jet_100 data.

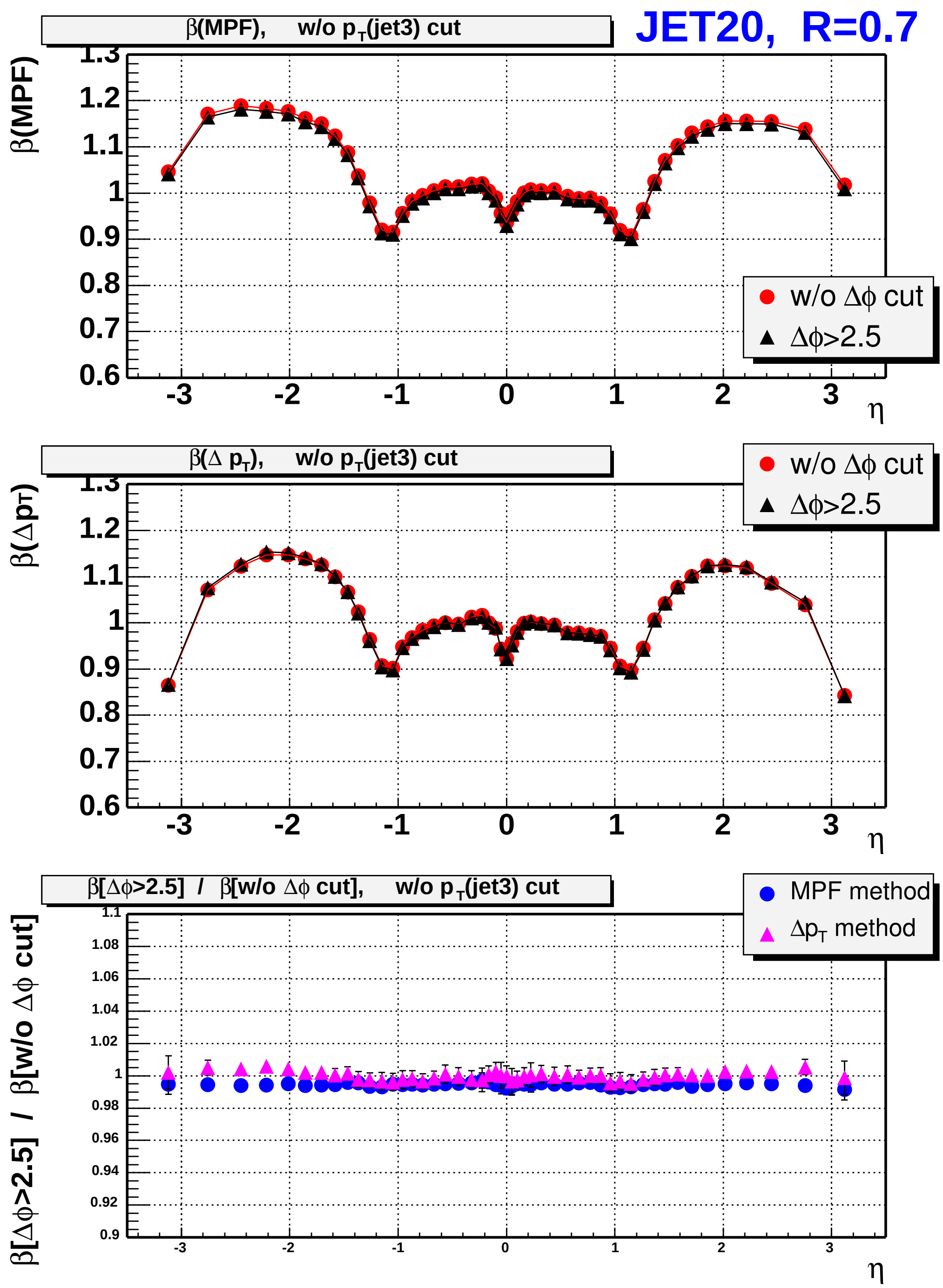

Figure 25: (top) $\beta(MPF)$ as a function of detector-η without any $\Delta\phi(jet1,2)$ cut (red circles) and with the $\Delta\phi(jet1,2) > 2.5$ (rad) cut (black triangles) for the Jet_20 data (cone size $R = 0.7$). No $p_T(jet3)$ cut is applied to these distributions. (middle) Same as (a) but for $\beta(\Delta p_T)$. (bottom) The ratio of β with the $\Delta\phi(jet1,2) > 2.5$ (rad) cut to that without the $\Delta\phi(jet1,2)$ cut as a function of detector-η for the MPF method (blue circles) and Δp_T method (magenta triangles).

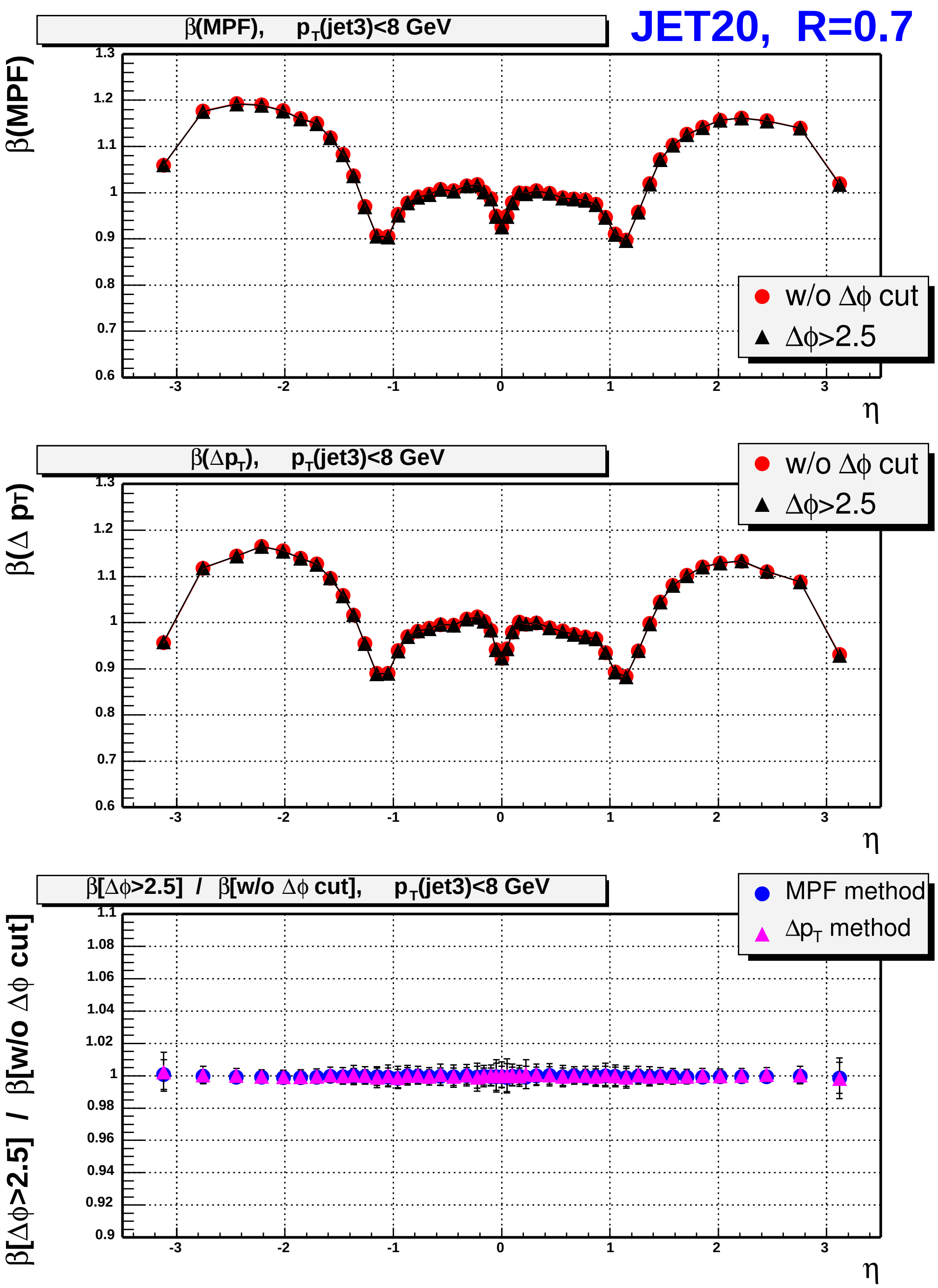

Figure 26: Same as plots in figure 25, but the $p_T(jet3) > 8$ GeV cut is applied to these distributions.

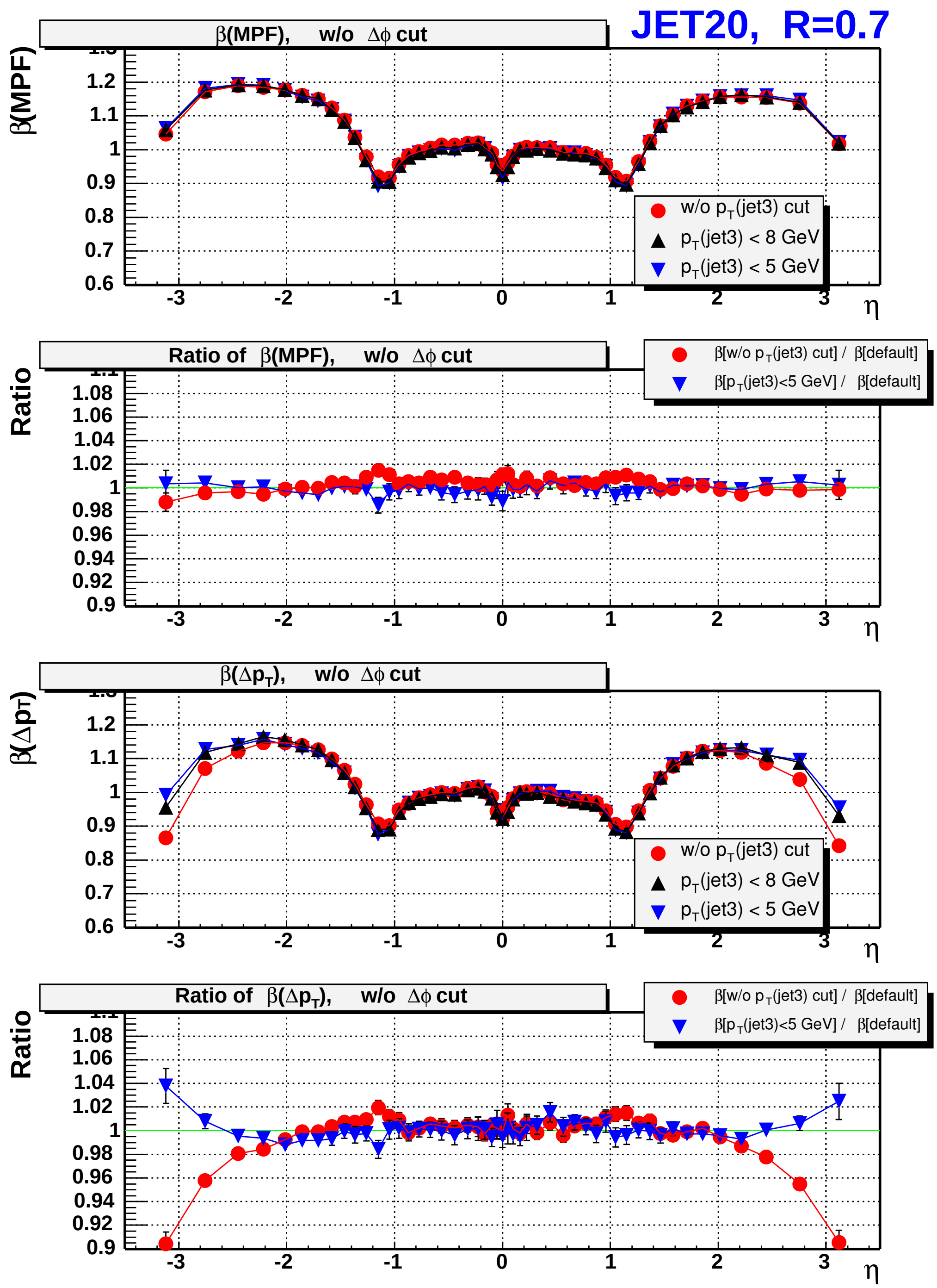

Figure 27: (a) $\beta(MPF)$ as a function of detector-η without any $p_T(jet3)$ cut (red circles), and with the $p_T(jet3) < 8$ GeV (black upward triangles) and 5 GeV (blue downward triangles) cuts for the Jet_20 data (cone size $R = 0.7$). The $\Delta\phi(jet1, 2) > 2.5$ (rad) cut is not applied to these distributions. (b) The ratio of $\beta(MPF)$ without any $p_T(jet3)$ cut to that with the $p_T(jet3) < 8$ GeV cut (red circles), and the ratio of $\beta(MPF)$ with the $p_T(jet3) < 5$ GeV cut to that with the $p_T(jet3) < 8$ GeV cut (blue triangles) as a function of detector-η. (c,d) same as (a,b) but for $\beta(\Delta p_T)$.

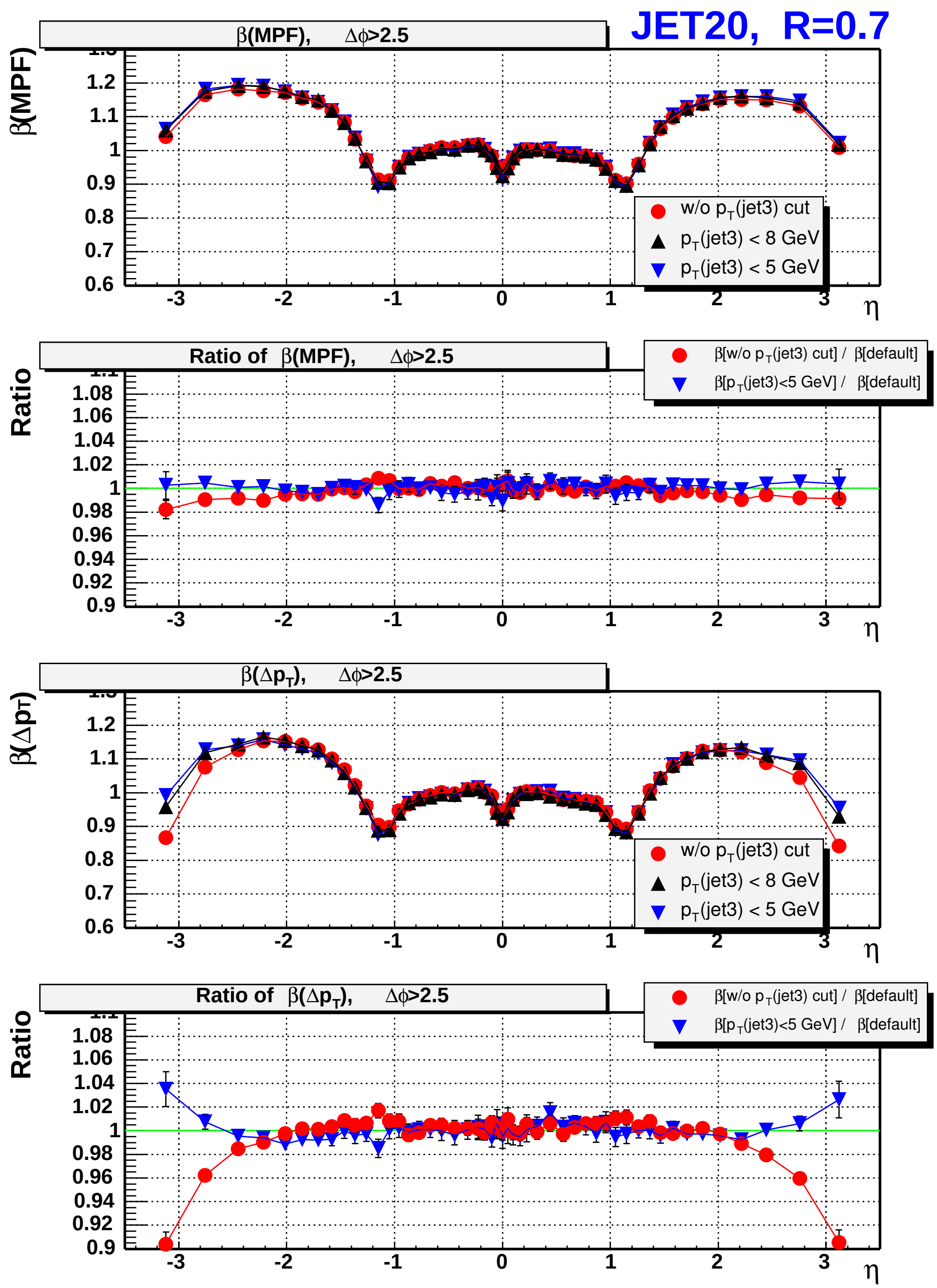

Figure 28: Same as plots in figure 27, but the $\Delta\phi(jet1,2) > 2.5$ (rad) cut is applied to these distributions.

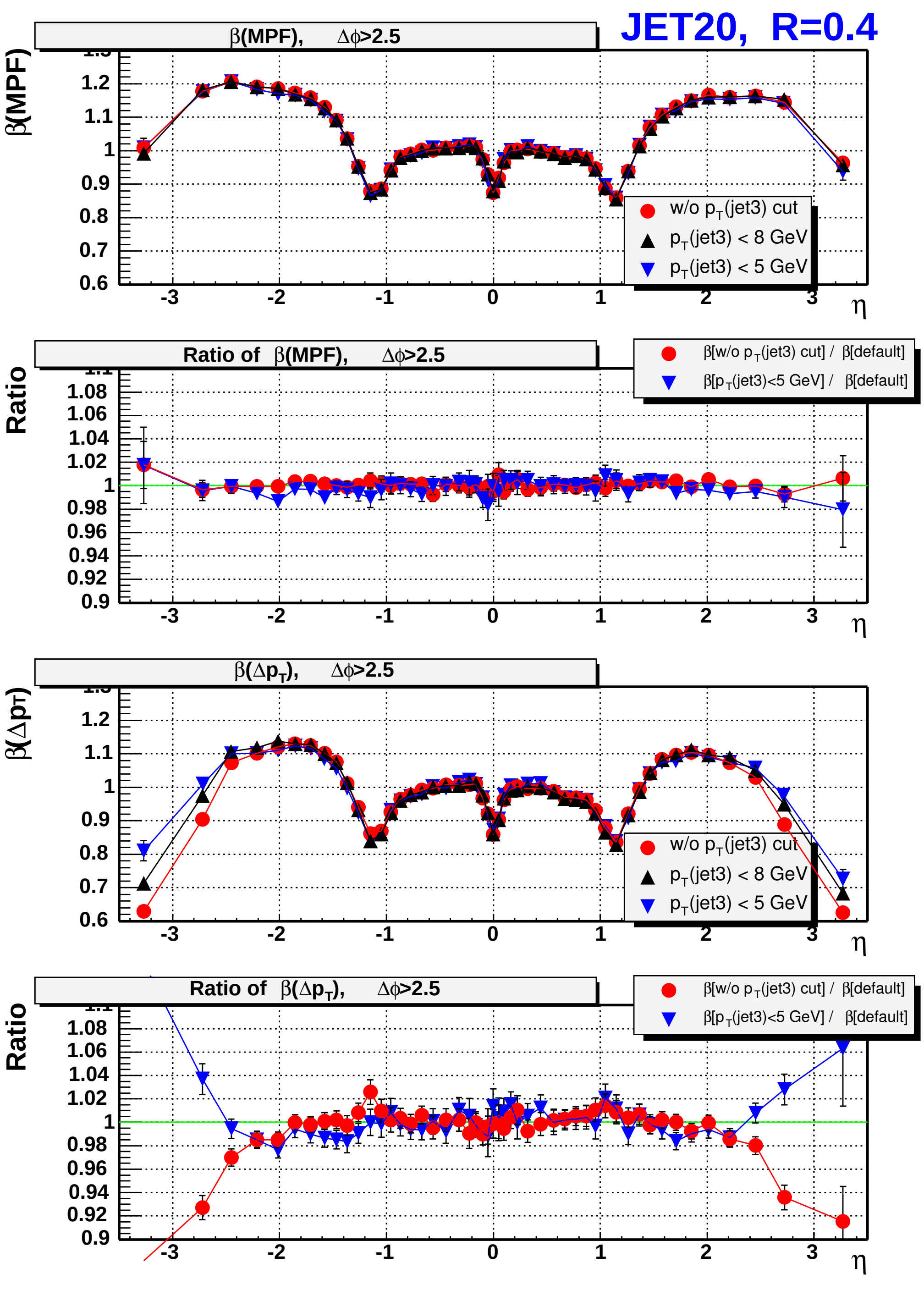

Figure 29: Same as plots in figure 28 but for the cone size $R = 0.4$.

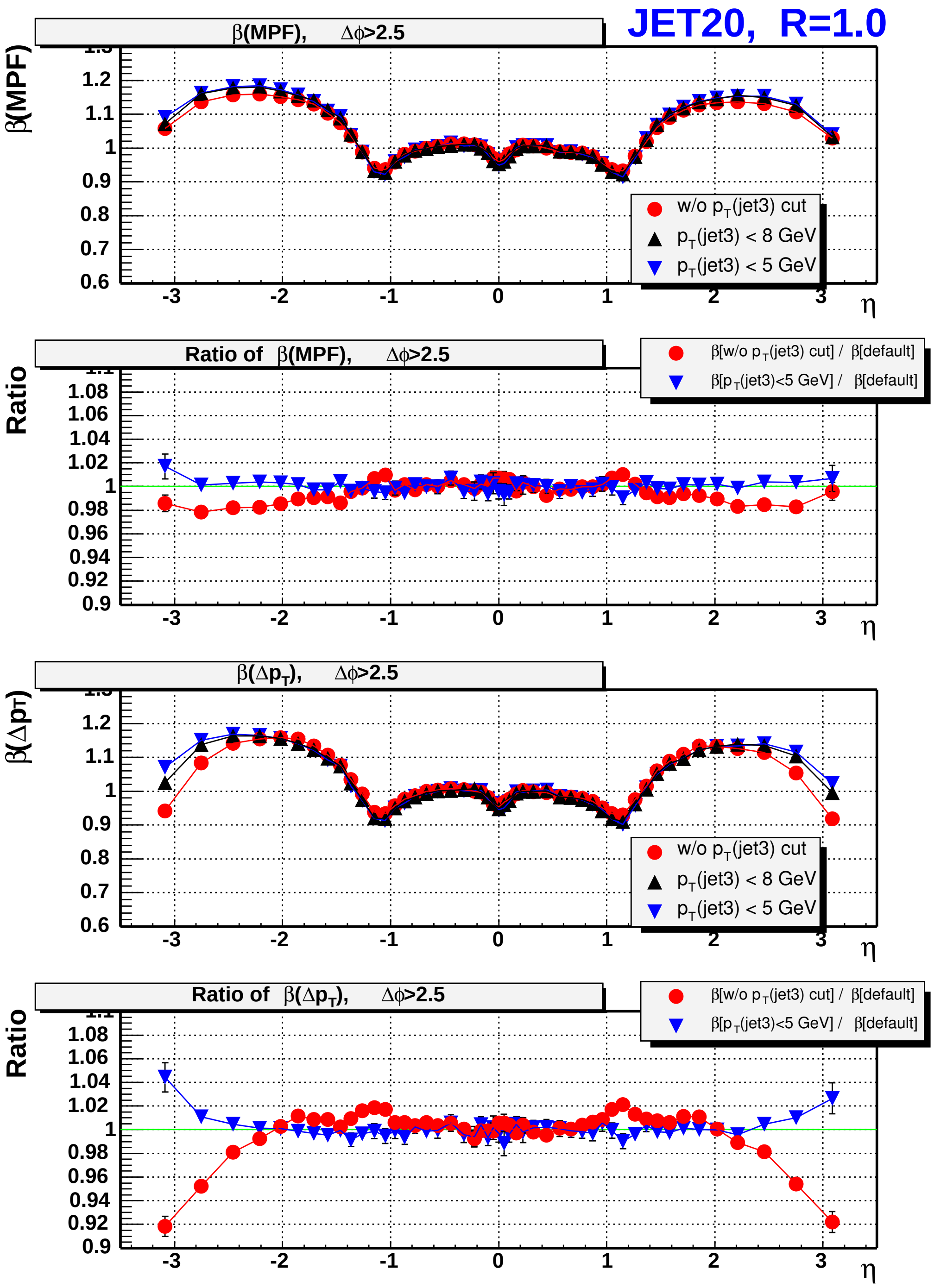

Figure 30: Same as plots in figure 28 but for the cone size $R = 0.4$.

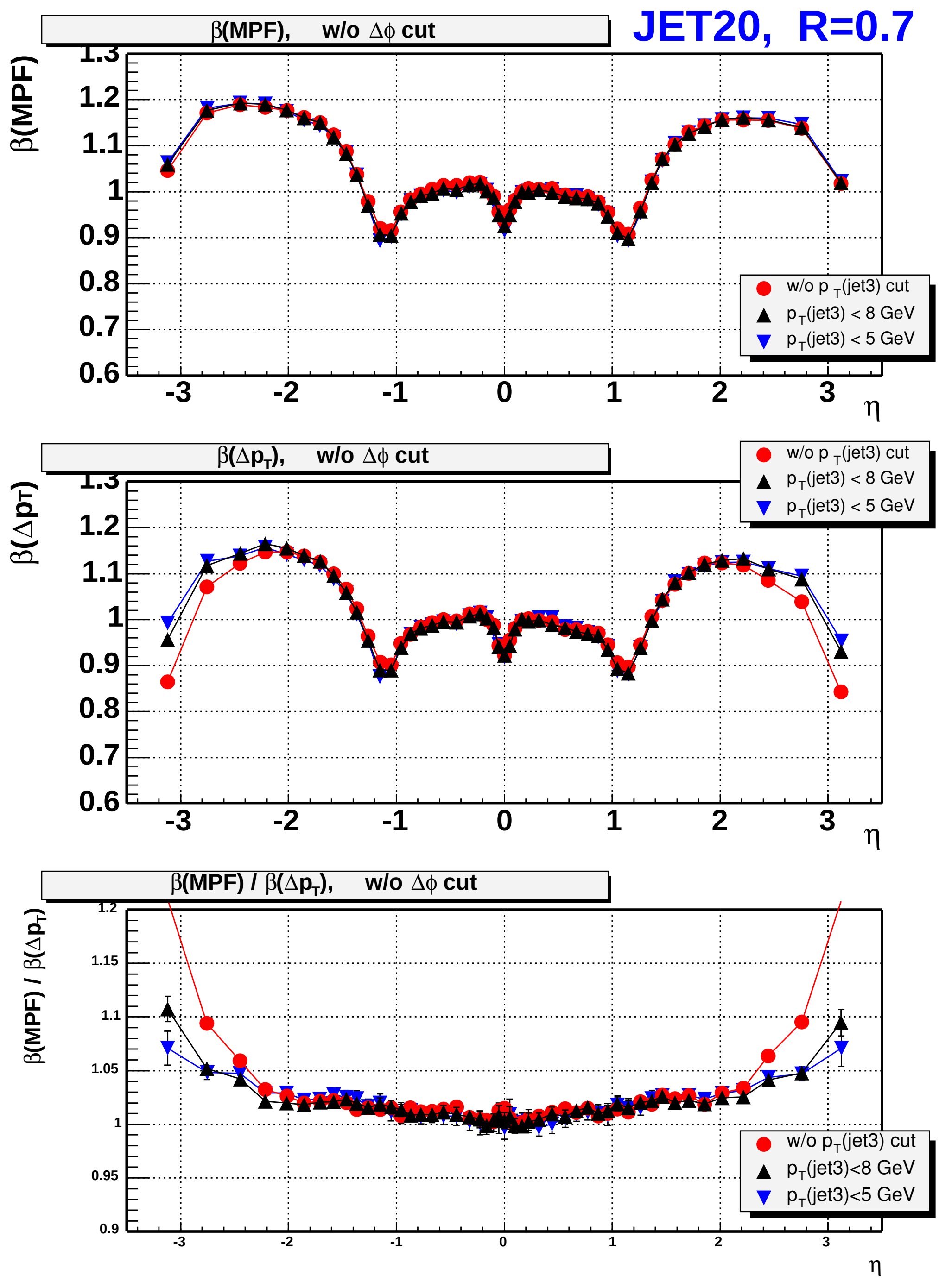

Figure 31: (a) $\beta(MPF)$ as a function of detector-η without any $p_T(jet3)$ (red circles) cut, and with the $p_T(jet3) < 8$ GeV (black upward triangles) and 5 GeV (blue downward triangles) cuts for the Jet_20 data (cone size $R = 0.7$). The $\Delta\phi(jet1, 2) > 2.5$ (rad) cut is not applied to these distributions. (b) Same as (a) but for $\beta(\Delta p_T)$. (b) The ratio of $\beta(MPF)$ to $\beta(\Delta p_T)$ as a function of detector-η without any $p_T(jet3)$ cut (red circles), with the $p_T(jet3) < 8$ GeV cut (black upward triangles), and with the $p_T(jet3) < 5$ GeV cut (blue downward triangles).

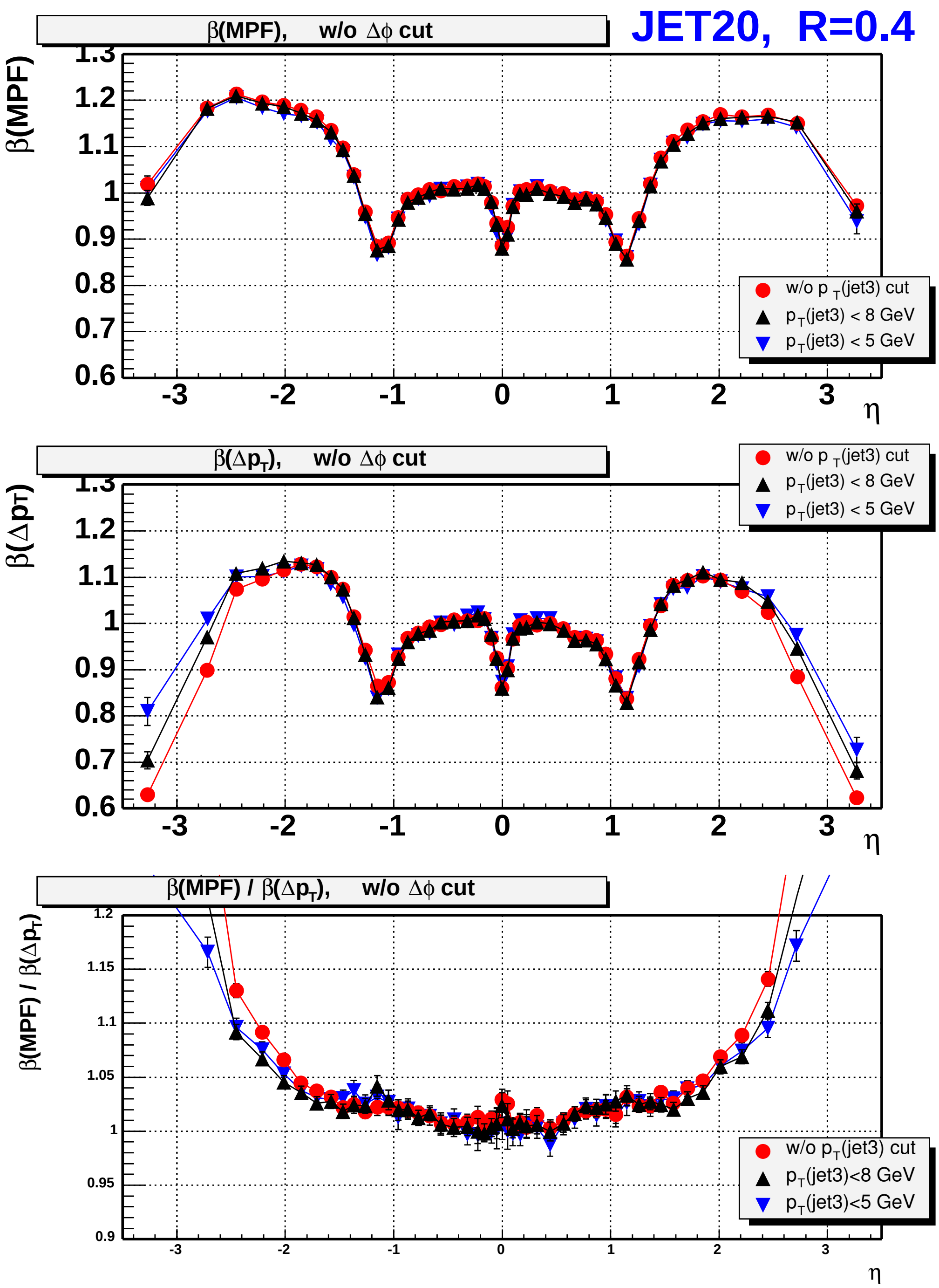

Figure 32: (a) $\beta(MPF)$ as a function of detector-η without any $p_T(jet3)$ (red circles) cut, and with the $p_T(jet3) < 8$ GeV (black upward triangles) and 5 GeV (blue downward triangles) cuts for the Jet_20 data (cone size $R = 0.4$). The $\Delta\phi(jet1, 2) > 2.5$ (rad) cut is not applied to these distributions. (b) Same as (a) but for $\beta(\Delta p_T)$. (b) The ratio of $\beta(MPF)$ to $\beta(\Delta p_T)$ as a function of detector-η without any $p_T(jet3)$ cut (red circles), with the $p_T(jet3) < 8$ GeV cut (black upward triangles), and with the $p_T(jet3) < 5$ GeV cut (blue downward triangles).

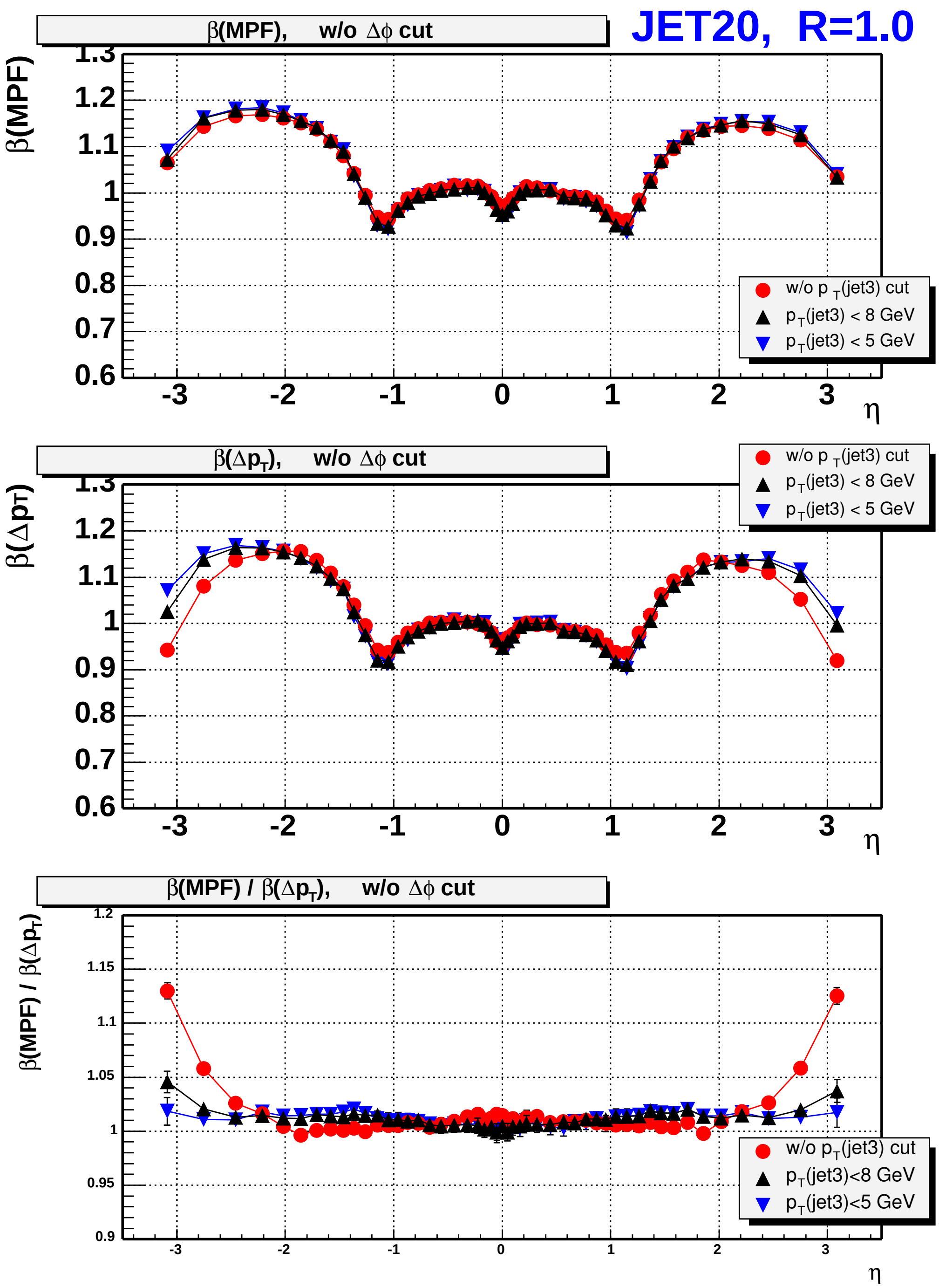

Figure 33: (a) $\beta(MPF)$ as a function of detector-η without any $p_T(jet3)$ (red circles) cut, and with the $p_T(jet3) < 8$ GeV (black upward triangles) and 5 GeV (blue downward triangles) cuts for the Jet_20 data (cone size $R = 1.0$). The $\Delta\phi(jet1, 2) > 2.5$ (rad) cut is not applied to these distributions. (b) Same as (a) but for $\beta(\Delta p_T)$. (b) The ratio of $\beta(MPF)$ to $\beta(\Delta p_T)$ as a function of detector-η without any $p_T(jet3)$ cut (red circles), with the $p_T(jet3) < 8$ GeV cut (black upward triangles), and with the $p_T(jet3) < 5$ GeV cut (blue downward triangles).

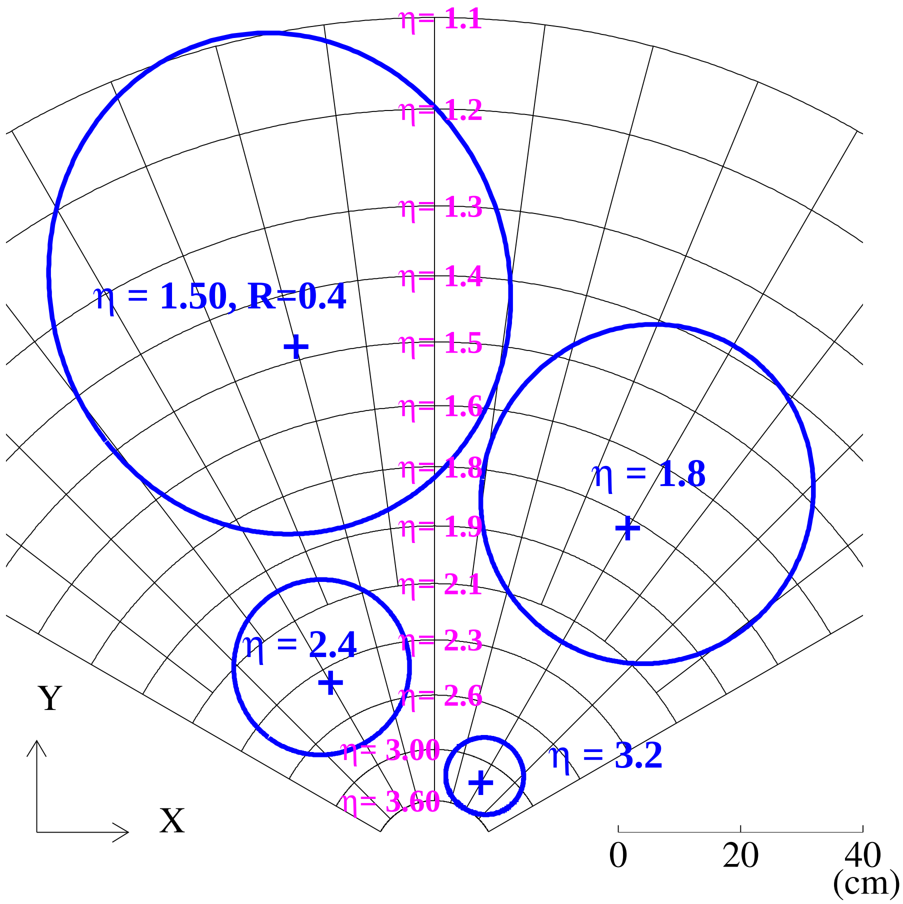

Figure 34: A view of the plug calorimeter in the X-Y plane. Jet cones of the size $R = \sqrt{\Delta\eta^2 + \Delta\phi^2} = 0.4$ are superimposed. Please note that jet cones with a fixed $R = \sqrt{\Delta\eta^2 + \Delta\phi^2}$ are much smaller in $X - Y$ space at higher $|\eta|$'s.

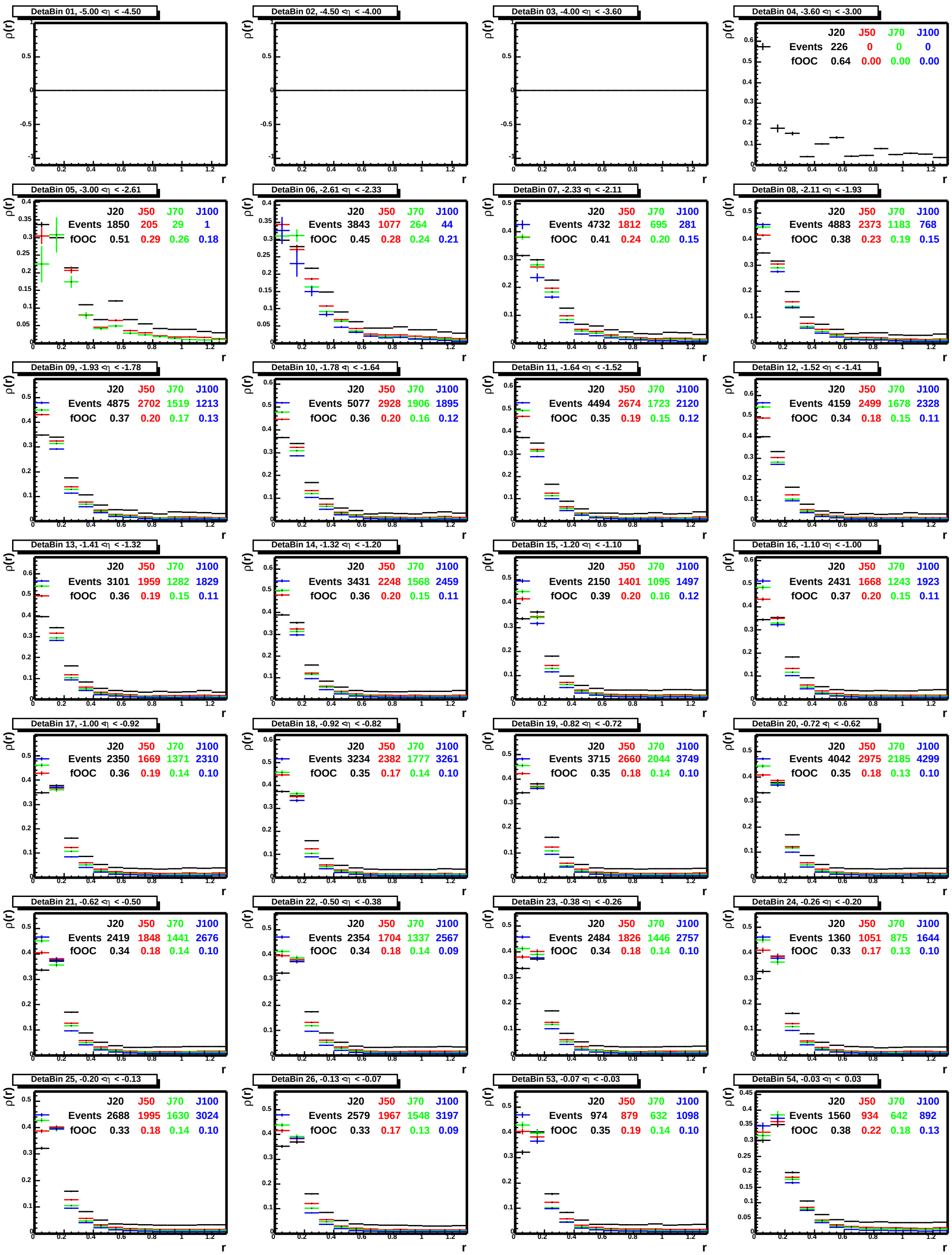

Figure 35: Distributions of $\rho(r)$ for the Jet_20, Jet_50, Jet_70 and Jet_100 data sets for detector-η bins on the negative η side.

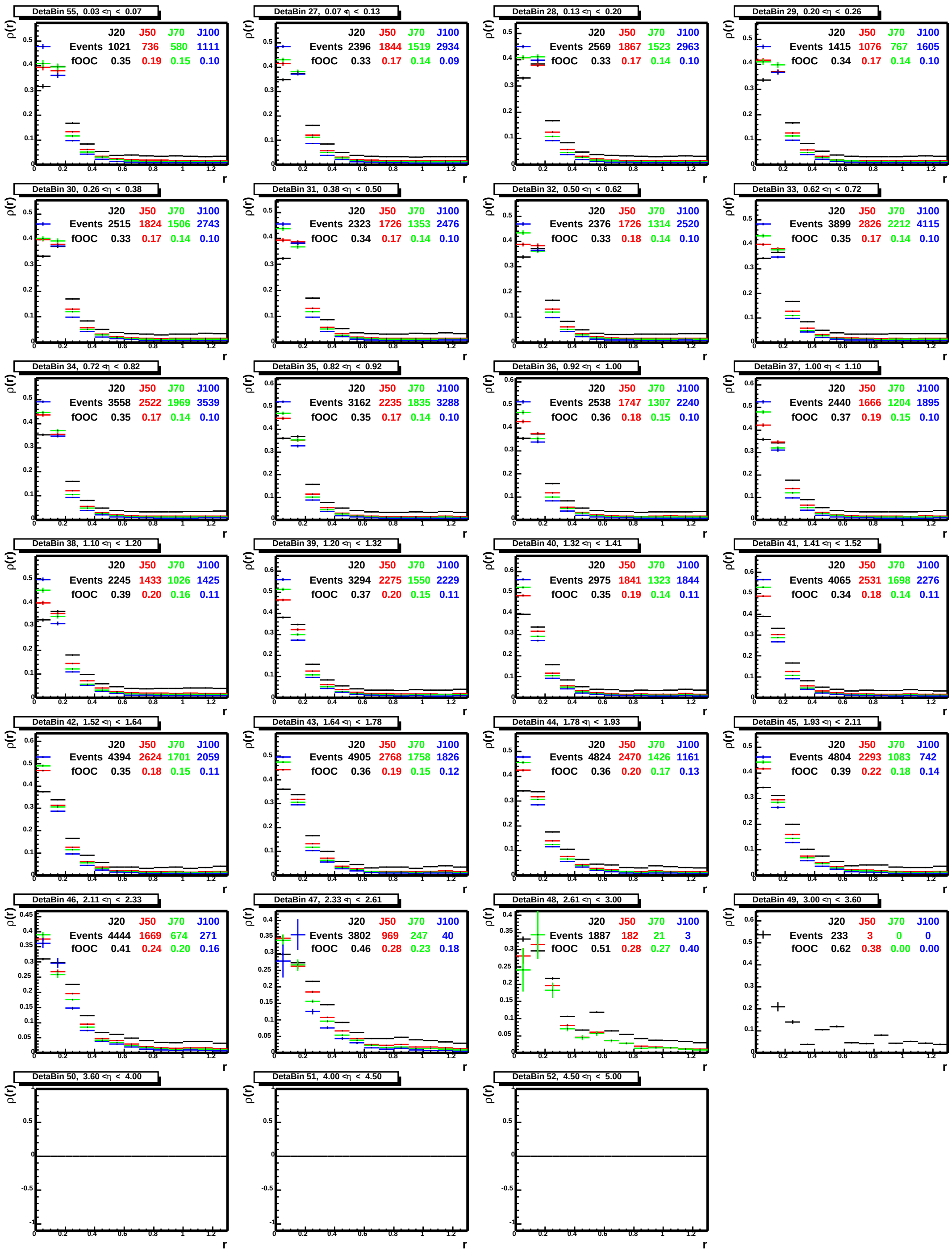

Figure 36: Distributions of $\rho(r)$ for the Jet_20, Jet_50, Jet_70 and Jet_100 data sets for detector-η bins on the positive η side.

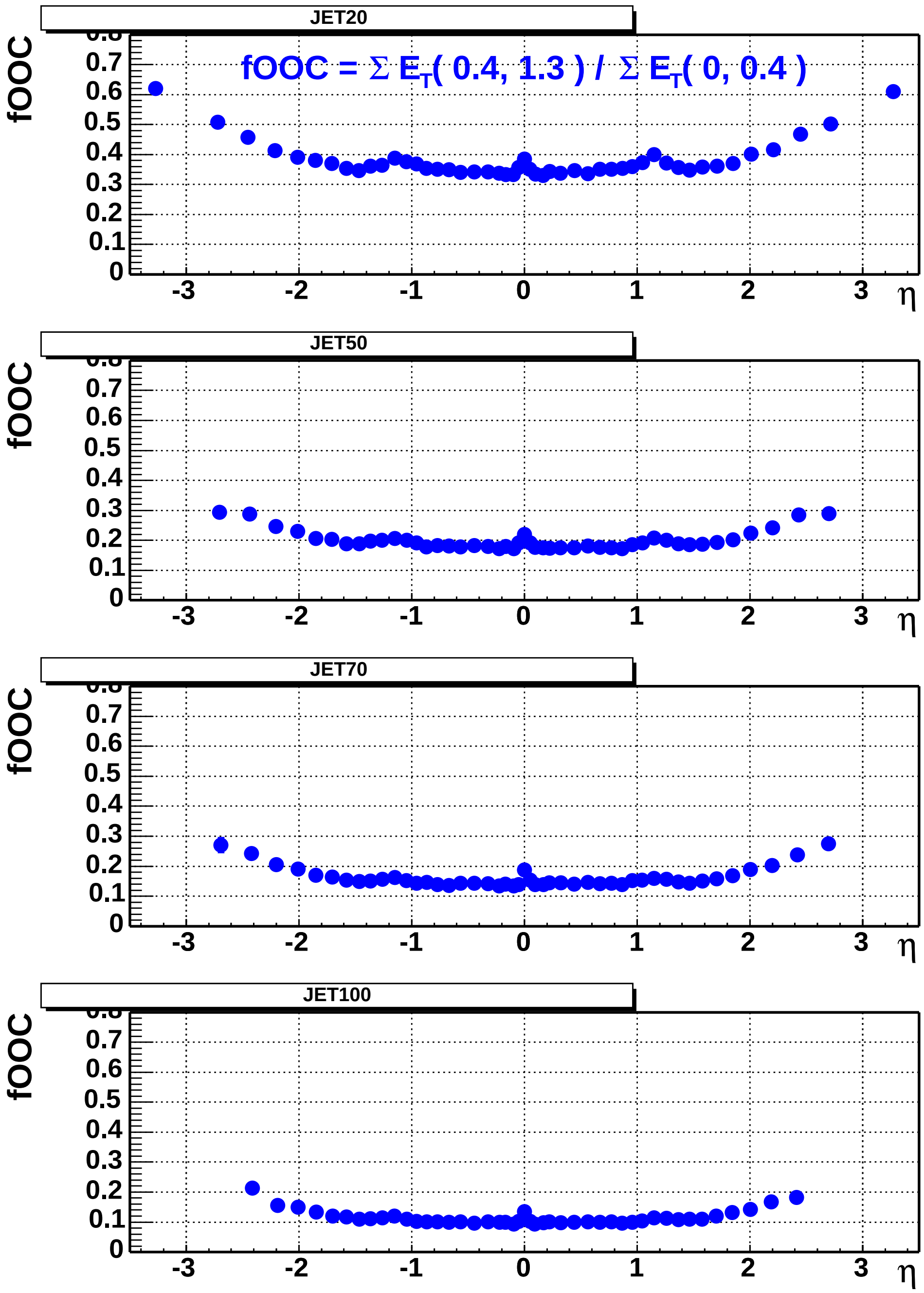

Figure 37: $fOOC$ as a function of detector-η for the cone size $R = 0.4$ for the Jet_20, 50, 70 and 100 data samples.

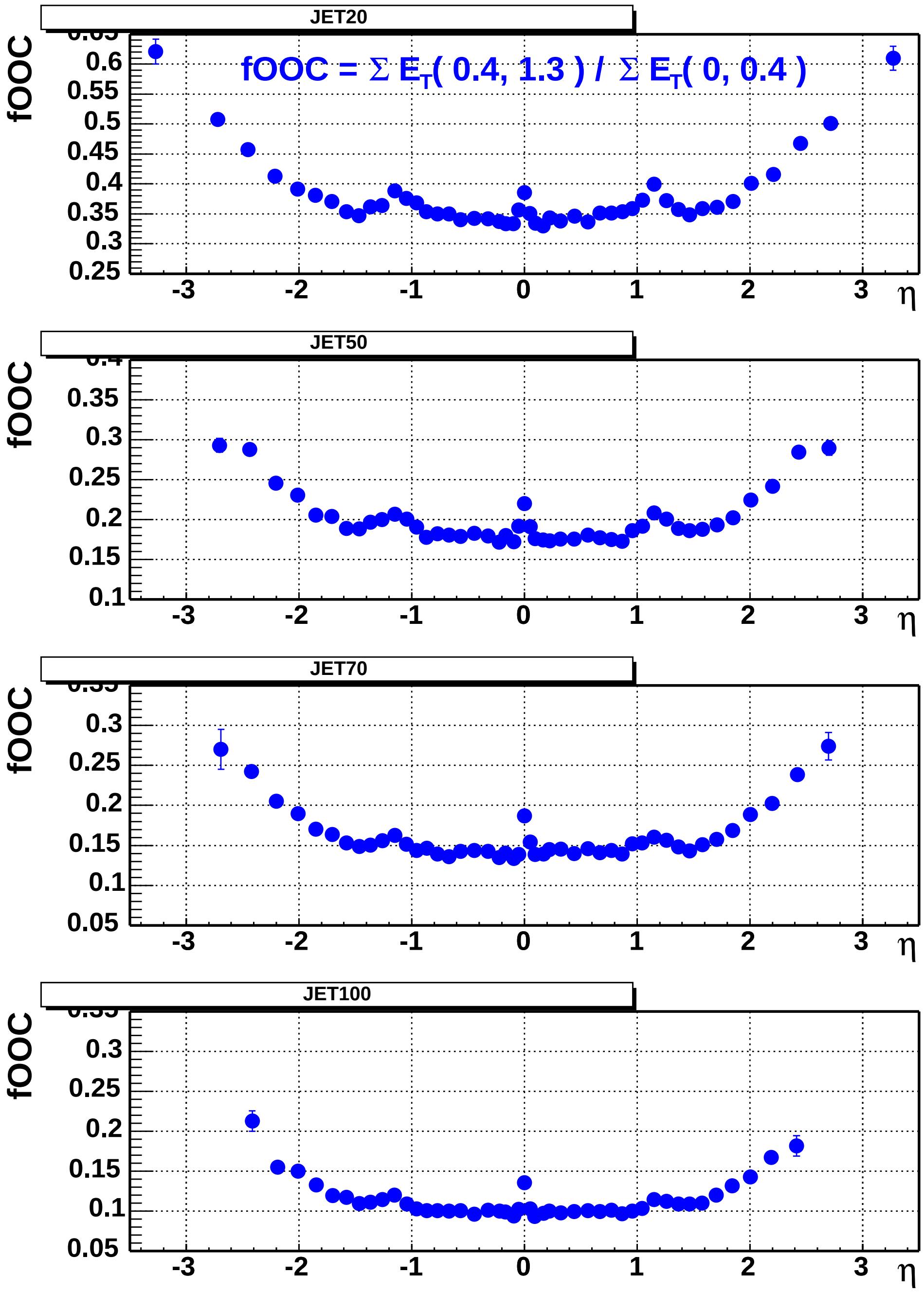

Figure 38: $fOOC$ as a function of detector-η for the cone size $R = 0.4$ for the Jet_20, 50, 70 and 100 data samples. The data points shown in this figure are the same as those in figure 37; however, the vertical scale of each plot is adjusted in this figure so that one can see the shape of the distributions better.

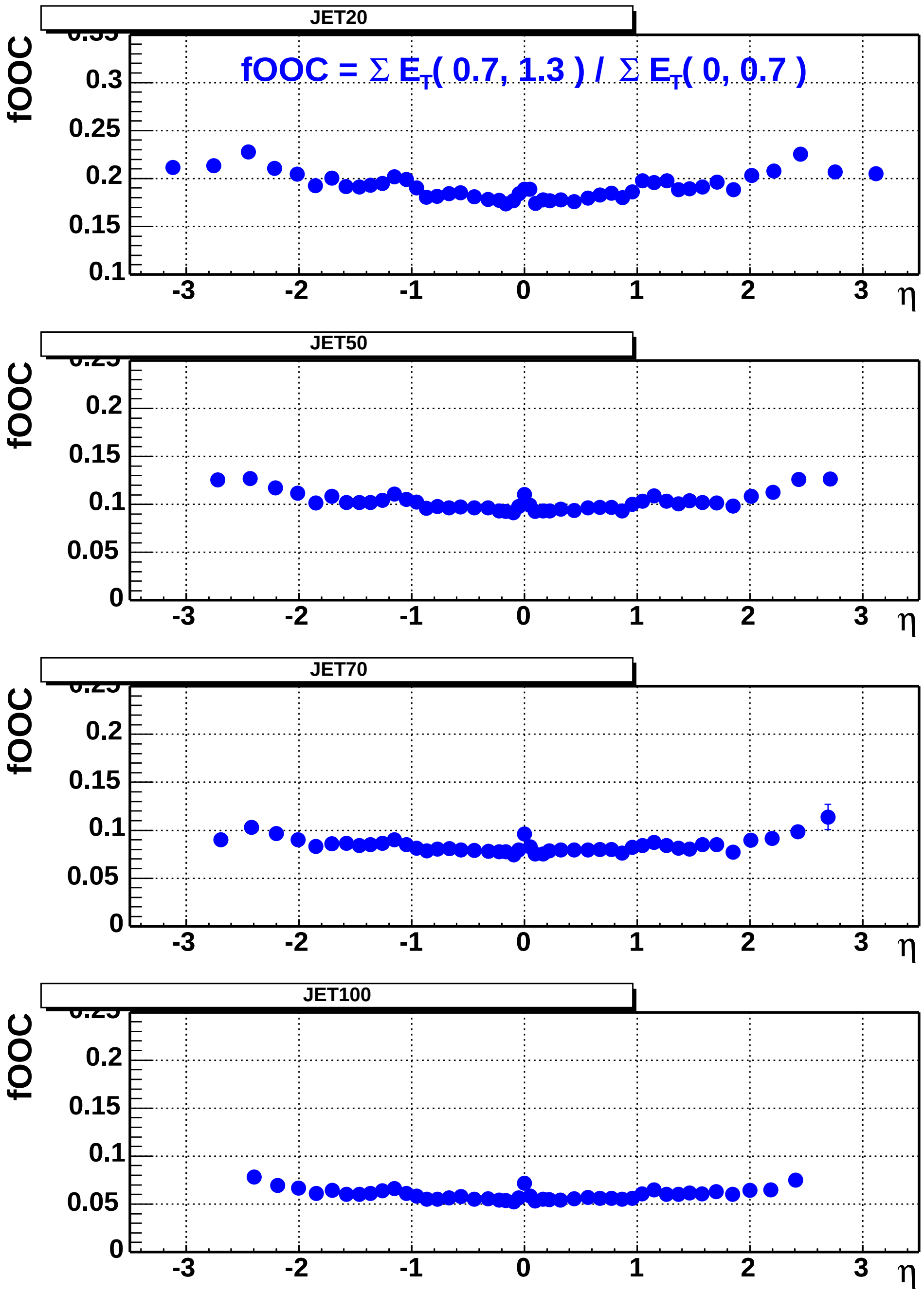

Figure 39: $fOOC$ as a function of detector-η for the cone size $R = 0.7$ for the Jet_20, 50, 70 and 100 data samples.

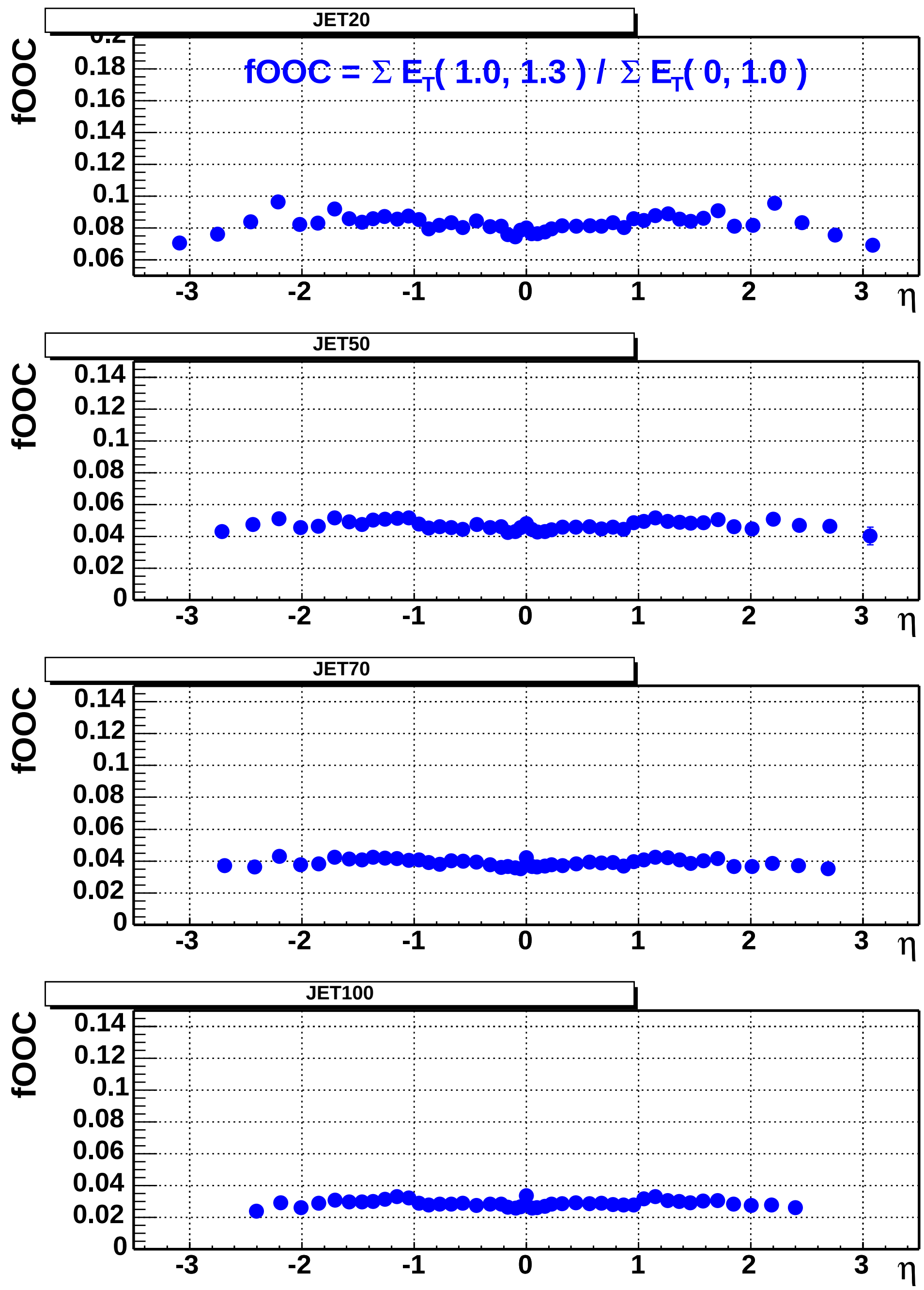

Figure 40: $fOOC$ as a function of detector-η for the cone size $R = 1.0$ for the Jet_20, 50, 70 and 100 data samples.